A novel flexible infinite element for transient acoustic simulations

D. Bizzarri, S. van Ophem, P. Marchner, O. Atak, H. Bériot

A novel flexible infinite element for transient acoustic simulations

D. Bizzarri[a,b,*], S. van Ophem[b,c], P. Marchner[a], O. Atak[d], H. Bériot[a]

[a] *Siemens Industry Software NV, Interleuvenlaan 68, Leuven, 3001, Belgium*
[b] *KU Leuven, Department of Mechanical Engineering, Celestijnenlaan 300, Heverlee, B-3001, Belgium*
[c] *Flanders Make@KU Leuven, Belgium*
[d] *Siemens Digital Industries Software, Hills Rd, Cambridge, United Kingdom*

Abstract

This article addresses the efficient solution of exterior acoustic transient problems using the Finite Element Method (FEM) in combination with infinite elements. Infinite elements are a popular technique to enforce non-reflecting boundary conditions. The Astley-Leis formulation presents several advantages in terms of ease of implementation, and results in frequency-independent system matrices, that can be used for transient simulations of wave propagation phenomena. However, for time-domain simulations, the geometrical flexibility of Astley-Leis infinite elements is limited by time-stability requirements. In this article, we present a novel infinite element formulation, called flexible infinite element, for which the accuracy does not depend on the positioning of the virtual sources. From a software implementation perspective, the element proposed can be seen as a specialized FEM element and can be easily integrated into a high-order FEM code. The effectiveness of the flexible formulation is demonstrated with frequency and time-domain examples; for both cases, we show how the flexible infinite elements can be attached to arbitrarily-shaped convex FE boundaries. In particular, we show how the proposed technique can be used in combination with existing model order reduction strategies to run fast and accurate transient simulations.

Keywords: Infinite elements, high-order FEM, transient acoustics,

*Corresponding author
Email address: davide.bizzarri@siemens.com (D. Bizzarri)

unbounded acoustics.

1. Introduction

The finite element method (FEM) is one of the most popular techniques to simulate the propagation of acoustic waves, as it allows to efficiently solve complicated problems by discretizing the physical domain of interest. The simulation of wave fields in unbounded regions represents a challenge, as computers can only handle a finite number of elements. The simplest, but rather inaccurate, approach consists of applying an impedance boundary condition at the artificial boundary of the finite element domain [1]. High-order absorbing boundary conditions [2] and the perfectly matched layer (PML) [3] represent more accurate alternatives. In particular, the PML has been proven to be very efficient for the solution of wave problems in the frequency domain. The PML has also been extensively studied for transient applications (see [4]-[10] and references therein). However, time-domain PML formulations require the use of auxiliary variables; the resulting increase in the number of degrees of freedom (DOFs) makes the PML less attractive to simulate transient phenomena.

The infinite element method, introduced by Bettess and Zienkiewicz [11], employs special elements that extend from the boundary of the FE domain to infinity. Over the years, different formulations have been proposed in the literature. In particular, two groups of formulations, which differ in the choice of the test functions in the infinite domain, were developed: the unconjugated formulation, where the test basis functions and the shape functions are the same, and the conjugated formulation, where the test basis functions are the complex conjugate of the shape functions. A detailed comparison of these strategies is given in [12], where the advantages and disadvantages of both are analyzed in detail.

Alternatives exist also in terms of geometrical discretization of the infinite elements. The so-called mapped formulations rely on a mapping from the physical element to a parent element [13]-[16]: their main advantage is the geometrical flexibility, as they can be attached to arbitrary convex-shaped FE boundaries. By contrast, for Burnett elements [17]-[19], the geometry of the envelope is restricted to spheroids and no mapping is employed.

Astley-Leis infinite elements [20] belong to the family of mapped formulations. They differ from other conjugated formulations by a weight factor in the test functions, which is designed to cancel out the unbounded

terms in the integrals that need to be computed to obtain the system matrices. Astley and Hamilton [21] studied the stability of these elements. For the standard Astley-Leis formulation, based on the Atkinson-Wilcox expansion [22], stability and convergence in the time domain have robustly been demonstrated only for configurations where the infinite elements are attached to spherical (or cylindrical) envelopes, with virtual sources aligning with a global center (or axis) of radiation. Under these conditions, the trial solution exhibits a close correspondence with a truncated form of the Atkinson-Wilcox expansion, leading to convergent solutions. A notable characteristic of these ideal configurations is that the global mass matrix of the infinite elements is theoretically zero for perfect spherical (or cylindrical) interfaces. However, practical implementations introduce discretization approximations, which can result in small, non-zero terms in the mass matrix. These minor deviations can potentially trigger spurious instabilities in transient simulations. The numerical studies reported in [21] indicate that stable solutions can be achieved by deliberately setting the global infinite element mass matrix to zero. This technique effectively disregards the small, non-zero contributions arising from discretization errors, without compromising the overall accuracy of the solution. When considering more general cases involving arbitrarily convex-shaped interior domains, a similar stability-preserving strategy can be employed. The key requirement for this approach is that the radial edges of the infinite elements must be normal to the finite element boundary. In such configurations, the infinite element mass matrix naturally approaches zero, allowing for the same technique of neglecting small discretization-induced contributions. However, in these cases, the virtual sources do not coincide with a global center of radiation, and, as a consequence, the trial solutions do not accurately approximate the global Atkinson-Wilcox expansion. In practice, for most scenarios, this means that standard Astley-Leis infinite elements based on the Atkinson-Wilcox expansion should be attached only to spherical (or cylindrical) envelopes for transient simulations.

Alternative mapped spheroidal infinite element formulations, based on the Holford expansion [18], have been proposed, both in the frequency domain and in the time domain [23], [24]. These elements were observed to give stable solutions without the need to set the infinite element mass matrix to zero [21]. However, for such formulations, as well as for non-mapped spheroidal formulations [17]-[19], the benefits of a smaller interior domain may be nullified by the necessary increases in the radial order of the infinite element shape functions, as observed in [24], [25] and [26].

Li et al. [27]-[30] proposed an alternative conjugated mapped formulation, where radial shape functions of the Lagrangian type are modified to satisfy exactly the truncated multipole expansion along the infinite edges, irrespective of the location of the virtual sources. However, to the best of the authors' knowledge, such formulation has not been explored in the context of transient simulations; additionally, it's worth noting that due to the restriction to radial shape functions derived from Lagrange polynomials, Li's elements may face challenges with conditioning, particularly for high radial orders [31].

The fact that conjugated infinite element formulations result in frequency-independent system matrices and maintain the sparsity of the FEM system, makes them readily available for time-domain simulations [32]-[34] and suitable for Model Order Reduction (MOR) [35]. This is particularly interesting, as in recent years MOR for transient simulations has emerged as one of the key technologies in a number of applications [36]-[39]. The aim of MOR techniques is to build Reduced Order Models (ROMs) that capture the most relevant dynamics of the corresponding initial Full Order Models (FOMs), using only a fraction of the DOFs. In [38] a numerical test is presented, for which the performance of the time-domain PML formulation from Kaltenbacher et al. [10] is compared with the Astley-Leis infinite element formulation. In particular, it is shown that using the PML results in a larger number of DOFs, due to the presence of the auxiliary variables. Moreover, from a MOR perspective, it is necessary to use a split-basis approach, which results in tripling the number of DOFs of the final ROM, to guarantee time-domain stability preservation of the PML formulation after MOR. Since this performance comparison between the PML and the infinite element method is limited to a single numerical test, it is difficult to draw general conclusions. The study cited, however, gives an indication that using infinite elements for unbounded transient problems leads to more efficient computations, especially when MOR techniques are used.

In this work, we propose a novel infinite element formulation for radial shape functions of any type, which satisfies exactly the truncated multipole expansion, irrespective of the orientation of the infinite edges. Consequently, we employ the new flexible infinite element to achieve a time-stable and accurate formulation, for arbitrarily shaped convex envelopes. Our approach retains the key advantages of standard Astley-Leis elements while extending applicability to more general geometries. Specifically, our formulation preserves the frequency-independent nature of the system matrices, main-

tains compatibility with standard quadrature rules for integral evaluation, and remains suitable for standard MOR techniques. The integration of the flexible infinite elements into a high-order FEM software is discussed. We show how one can take advantage of the quickhull algorithm [40] to automatically generate a convex acoustic domain around sources of interest. Finally, the combination of the proposed formulation with an existing MOR strategy is discussed.

The article is structured as follows. In Section 2, the Helmholtz problem and the resulting system of equations in the time domain are introduced, together with a description of the standard Astley-Leis formulation. In Section 3, the novel flexible infinite element is presented and its stability properties are discussed. In Section 4, we discuss the integration of the infinite element formulation into a high-order FEM software. In Section 5, we demonstrate the effectiveness of the proposed method on two academic examples, while in Section 6 we consider a problem of industrial complexity. Finally, a conclusion is proposed in Section 7.

2. Finite and Infinite elements for acoustics

This section provides the theoretical background for our study of the flexible infinite element formulation. We first introduce the notation and provide an overview of the general problem in Section 2.1. We then review the state-of-the-art formulation, namely the Astley-Leis infinite elements, in Section 2.2. Finally, in Section 2.3, we review the conditions for the stability of the Astley-Leis formulation and discuss its limitations in the context of transient simulations. These limitations provide the motivation for the development of the flexible infinite element formulation.

2.1. Problem statement

2.1.1. Governing equation

We take the convention that the time-dependence of the fields is $\exp(\mathrm{i}\omega\tau)$, where ω is the angular frequency and τ is the time. The behavior of the pressure field p in the unbounded domain Ω is described by the Helmholtz equation in the frequency domain:

$$\nabla^2 p + k^2 p = 0 \quad \text{in } \Omega, \tag{1}$$

where k is the wavenumber. The domain Ω is subdivided into an interior region Ω_i and an exterior region Ω_e; we denote with Γ the interface between the two domains (see Figure 1).

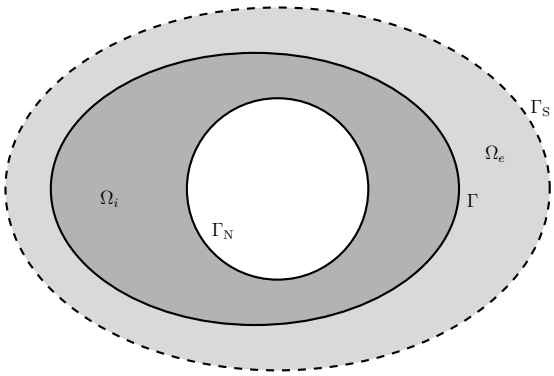

Figure 1: Exterior acoustic problem, schematic representation. Ω_i and Ω_e are the interior and exterior domain, respectively. Γ is the interface between the two domains, and Γ_S is the envelope where the Sommerfeld condition is imposed.

At the interior boundary Γ_N of the domain Ω_i a Neumann boundary condition is prescribed. Dirichlet and Robin boundary conditions can be easily handled as well, but they won't be considered here for ease of notation. The Sommerfeld condition states that no waves can be reflected at infinity; in mathematical terms, in a d dimensional domain, this is written as:

$$r^{\frac{d-1}{2}} \left\{ \frac{\partial p}{\partial r} + \mathrm{i}kp \right\} \to 0 \quad \text{as} \quad r \to \infty, \tag{2}$$

where r is the spherical/cylindrical radius.

As in [41], approximating (2), we can rewrite:

$$\nabla_x p \cdot \mathbf{n} = -\mathrm{i}kp \quad \text{on} \quad \Gamma_S, \tag{3}$$

where ∇_x is the gradient operator in Cartesian coordinates, and Γ_S is a spherical (or cylindrical) envelope with outward unit normal $\mathbf{n}$, placed at radial distance R from the envelope Γ, with $R \to \infty$.

The corresponding boundary value problem reads as follows:

$$\begin{cases} \nabla^2 p + k^2 p = 0 \text{ in } \Omega \\ \nabla_x p \cdot \mathbf{n} = -\mathrm{i}\rho\omega v_n \text{ on } \Gamma_N \\ \nabla_x p \cdot \mathbf{n} = -\mathrm{i}kp \text{ on } \Gamma_S, \text{ for } R \to \infty, \end{cases} \tag{4}$$

where ρ is the fluid density and v_n is the prescribed normal velocity on Γ_N.

2.1.2. Variational formulation and discretization

Using the method of weighted residuals, we obtain the following variational formulation:

$$\left| \begin{array}{l} \text{Find } p \in H^1(\Omega) \text{ such that, } \forall q \in H^1(\Omega) \\ \lim\limits_{R\to\infty} \displaystyle\int_\Omega \left\{ \nabla_x q \cdot \nabla_x p - k^2 q p \right\} \mathrm{d}\Omega + \mathrm{i}k \int_{\Gamma_\mathrm{S}} \{qp\} \, \mathrm{d}\Gamma + \mathrm{i}\omega \int_{\Gamma_\mathrm{N}} \{\rho q v_n\} \, \mathrm{d}\Gamma = 0, \end{array} \right. \tag{5}$$

where H^1 is the Sobolev space where the solution is sought.

Eq. (5) is solved by using H^1-conforming finite elements in Ω_i and attaching infinite elements to the envelope Γ. In this case, p and q are approximated by $p^h \in V^h \subset H^1(\Omega)$ and $q^h \in Q^h \subset H^1(\Omega)$, where V^h is the space of shape functions and Q^h is the space of test functions. In the Astley-Leis formulation, thanks to the weight factor used in the test functions, the Sommerfeld condition is automatically satisfied and does not need to be taken into account in the variational formulation [20]. The discrete variational formulation reads:

$$\left| \begin{array}{l} \text{Find } p^h \in V^h \text{ such that, } \forall q^h \in Q^h \\ \lim\limits_{R\to\infty} \displaystyle\int_\Omega \left\{ \nabla_x q^h \cdot \nabla_x p^h - k^2 q^h p^h \right\} \mathrm{d}\Omega + \mathrm{i}\omega \int_{\Gamma_\mathrm{N}} \left\{ \rho q^h v_n \right\} \mathrm{d}\Gamma = 0, \end{array} \right. \tag{6}$$

which can be rewritten as a linear system of equations:

$$\left[-\omega^2 \mathbf{M} + i\omega \mathbf{C} + \mathbf{K} \right] \mathbf{p}(\omega) = \mathbf{f}(\omega), \tag{7}$$

where $\mathbf{p}$ is the vector of DOFs, $\mathbf{f}$ is the forcing vector, $\mathbf{M}$, $\mathbf{C}$, and $\mathbf{K} \in \mathbb{R}^{n_\mathrm{DOF} \times n_\mathrm{DOF}}$ are the mass, damping, and stiffness matrices, respectively, and n_DOF is the number of DOFs.

Since, for the Astley-Leis formulation, the system matrices are frequency-independent, Eq. (7) can be readily transformed into the time domain:

$$\mathbf{M}\ddot{\mathbf{p}}_{\boldsymbol{\tau}}(\tau) + \mathbf{C}\dot{\mathbf{p}}_{\boldsymbol{\tau}}(\tau) + \mathbf{K}\mathbf{p}_{\boldsymbol{\tau}}(\tau) = \mathbf{f}_{\boldsymbol{\tau}}(\tau), \tag{8}$$

where $\mathbf{p}_{\boldsymbol{\tau}}$ and $\mathbf{f}_{\boldsymbol{\tau}}$ are the inverse Fourier transforms of $\mathbf{p}$ and $\mathbf{f}$, respectively.

2.1.3. Multipole expansion

The Atkinson-Wilcox theorem [22] states that at any point outside the smallest sphere circumscribing all the sound sources, the solution of problem

(4) can be written as the multipole expansion:

$$p = \exp(-\mathrm{i}kr) \sum_{n=1}^{\infty} \frac{G_n(\alpha, \theta, k)}{r^n} \tag{9}$$

where G_n is the directivity function, α and θ are the spherical angles, and r is the radial distance, measured from the center of radiation, that coincides with the center of the minimal enclosing sphere. For ease of notation, throughout the rest of the paper, we will assume that the origin O of the absolute Cartesian coordinate system coincides with the center of radiation.

The Atkinson-Wilcox theorem has been extended by Burnett and Holford [18] to include the spheroidal case. By placing the envelope Γ outside the minimal enclosing sphere (for the Atkinson-Wilcox expansion) or spheroid (for the Holford expansion), we ensure that the solution in the exterior domain Ω_e is composed only of outward propagating waves; this consideration is used to select a proper trial solution in the infinite elements.

The so-called spheroidal formulations have received some criticism in the past [24]-[26], since the smaller number of DOFs in the FEM region is often counterbalanced, in practical applications, by the need for higher radial orders in the exterior region. On the other hand, numerical experiments have been performed in the frequency domain, using mapped infinite elements based on expansion (9), where the conditions of the Atkinson-Wilcox theorem were explicitly violated [42], [31], [43]: namely, non-spherical envelopes were used, partially lying inside the minimal enclosing sphere. Although the convergence of this approach has not been formally proven [44], numerical experiments with sufficiently smooth envelopes gave satisfactory results (see [45] for more details). For all the test cases encountered during our research, our observations were in line with the cited literature. These claims will be further expanded in Section 6.

2.2. Review of Astley-Leis infinite elements

2.2.1. Geometrical interpolation

The Astley-Leis formulation relies on a mapping from the infinite physical element to a finite parent element. In particular, in two dimensions (see Figure 2), the physical element is mapped to a rectangular parent element (t, $v \in [-1, 1]$); in three dimensions, the parent element can be a triangular prism or a cube, depending on the shape of the corresponding physical element, and the parent element coordinates are named s, t and v.

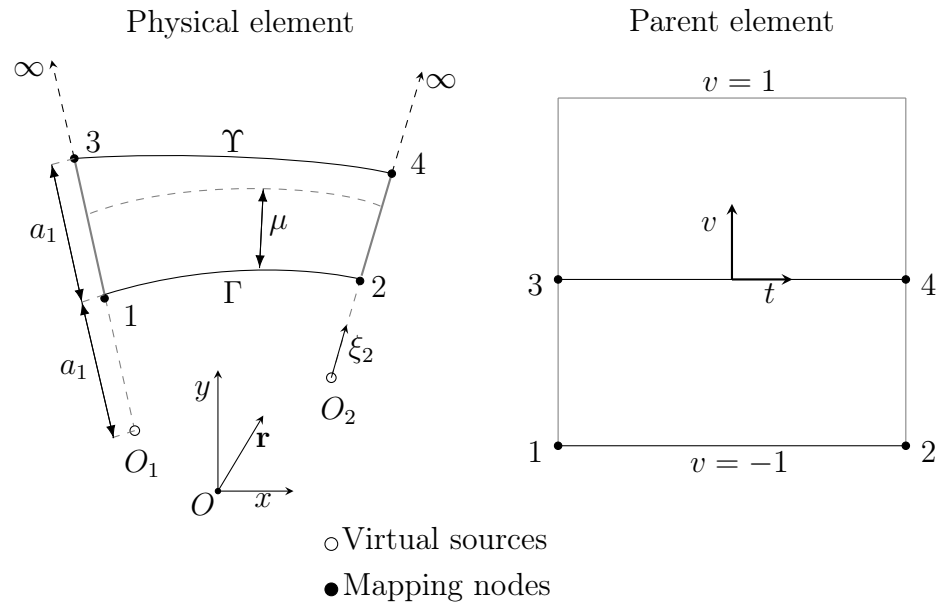

Figure 2: Schematic representation of a mapped infinite element. In our convention, the center of radiation coincides with the origin O of the Cartesian coordinates system.

In the following, we denote the position vector of the generic point p in the e-th infinite element by the vector of Cartesian coordinates $\mathbf{x}_p = (x_p, y_p, z_p)$. During the meshing process of the interior domain, n nodes are defined on the envelope Γ within the e-th infinite element. Subsequently, for each node on Γ, a corresponding mapping node is defined in the exterior domain. The i-th infinite edge is the line that originates from node i on Γ, passes through the corresponding mapping node $i + n$, and extends to infinity (see Figure 2).

We denote with a_i the distance between the mapping nodes i and $i + n$:

$$a_i = ||\mathbf{x}_{i+n} - \mathbf{x}_i|| \,, \tag{10}$$

where $||\cdot||$ is the Euclidean norm. The virtual source O_i is located (see Figure 2) along the direction of the i-th infinite edge, towards the interior domain, at distance a_i from Γ.

For any point on the i-th infinite edge, the distance ξ_i from the corresponding virtual source is mapped to the parent element radial coordinate v:

$$\xi_i(v) = \frac{2a_i}{1 - v}. \tag{11}$$

We denote with ξ the interpolated distance between the mapping nodes and their corresponding virtual sources. A mapping between ξ and the radial parent element coordinate v is obtained for any point inside the infinite element:

$$\xi(s,t,v) = \frac{2\,a(s,t)}{1-v}, \tag{12}$$

where the interpolated distance a between the mapping nodes on Γ and their respective virtual sources is defined as:

$$a(s,t) = \sum_{i=1}^{n} {N_t}^i(s,t) a_i. \tag{13}$$

where ${N_t}^i$ are the standard tangential geometrical mapping functions (typically Lagrangian polynomials).

The vector of Cartesian coordinates for a point inside the e-th infinite element is found by interpolating the nodal Cartesian coordinates:

$$\mathbf{x}(s,t,v) = N_v^{\Gamma}(v) \sum_{i=1}^{n} {N_t}^i(s,t)\mathbf{x}_i + N_v^{\Upsilon}(v) \sum_{i=1+n}^{2n} {N_t}^i(s,t)\mathbf{x}_i, \tag{14}$$

where $\mathbf{x}_i$ are the vectors of Cartesian coordinates at the mapping nodes, and the radial geometric mapping functions $N_v^{\Gamma}(v)$ and $N_v^{\Upsilon}(v)$ are defined as:

$$N_v^{\Gamma}(v) = \left(-\frac{2v}{1-v}\right), \quad N_v^{\Upsilon}(v) = \left(\frac{1+v}{1-v}\right). \tag{15}$$

Finally, the so-called phase distance μ is defined as:

$$\mu(s,t,v) = \xi(s,t,v) - a(s,t). \tag{16}$$

When the infinite edges are extruded orthogonally to Γ, the phase distance $\mu\,(s,t,v)$ represents the distance between the point with physical coordinates $\mathbf{x}\,(s,t,v)$ and the envelope Γ, as represented in Figure 2.

We emphasize that the notation adopted here is slightly different from what is usually found in the literature because we want to distinguish between r as defined in Section 2.1.3 (i.e., the distance from the center of radiation) and ξ, the interpolated distance between the mapping nodes and their respective virtual sources, defined in (12). In particular, since we take the convention that the origin O of the Cartesian coordinate system coincides with the center of radiation, r can be written as:

$$r(s,t,v) = \|\mathbf{x}(s,t,v)\|. \tag{17}$$

2.2.2. Shape and test functions

By analogy with the Atkinson-Wilcox expansion (9), the shape functions are written as:

$$\boldsymbol{\Phi}(s,t,v) = \boldsymbol{\Psi}(s,t,v)\exp\left[-\mathrm{i}k\mu\right], \tag{18}$$

where $\boldsymbol{\Psi}(s,t,v)$ is the usual vector of polynomial shape functions used in the FE domain. By inserting the radial mapping (12) in (18), it can be verified that the trial solution $\tilde{p}$ in the exterior domain takes the following form:

$$\tilde{p} \sim \left(\frac{\alpha_1}{\xi} + ... + \frac{\alpha_m}{\xi^m}\right)\exp\left[-\mathrm{i}k(\xi - a)\right], \tag{19}$$

where m is the selected radial order in the infinite domain, and the terms $\alpha_1, ..., \alpha_m$ are interpolation functions

$$\alpha_i = \alpha_i(s,t)\,\forall i \in [1,m]. \tag{20}$$

In other words, for the i-th infinite edge, the pressure field generated by the m-th order virtual multipole source, placed at O_i, can be accurately approximated. This is where the idea of virtual sources comes from.

An interesting case to analyze is when all the virtual sources of the e-th infinite element coincide with the center of radiation O. In this case, along the i-th infinite edge, we obtain:

$$\tilde{p} \sim \left(\frac{\alpha_1}{r} + ... + \frac{\alpha_m}{r^m}\right)\exp\left[-\mathrm{i}k(r - a)\right], \tag{21}$$

since $\xi = r$ along the i-th infinite edge, when $O_i \equiv O$. In other words, when all the virtual sources coincide with the center of radiation, the approximated field variable p^h can mimic the multipole expansion (9), truncated at the radial order m, along the infinite edges, ensuring good accuracy of the approximation. In all other cases, relationship (21) is not necessarily true. This explains why, for traditional mapped infinite element formulations, the accuracy depends on the location of the virtual sources.

In the Astley-Leis formulation, a Petrov-Galerkin approach is taken: the test and trial functions belong to different function spaces; in particular, the test basis functions are the complex conjugate of the shape functions, multiplied by a weight factor w:

$$\widetilde{\boldsymbol{\Phi}} = w\boldsymbol{\Psi}\exp[+\mathrm{i}k\mu], \tag{22}$$

where the weight factor takes the form:

$$w = \left(\frac{1 - v}{2} \right)^{p_w} . \tag{23}$$

In contrast to the Bubnov-Galerkin method, where the test basis functions are equal to the shape functions, the Petrov-Galerkin method results in unsymmetric system matrices. This choice for the test basis functions is particularly convenient: first, being a conjugated formulation, the Astley-Leis formulation results in frequency-independent system matrices, which can be readily used in the time domain; second, for $p_w \geq 2$, standard quadrature rules can be used for the evaluation of the integrals necessary to compute the system matrices. In [20] the choice of $p_w = 2$ is justified on physical grounds, although it is pointed out that any power $p_w \geq 2$ preserves the boundedness of the system matrix integrals. Irrespective of the choice of p_w, the conjugated weighted formulation was shown to lead to a variational formulation in weighted Sobolev spaces, for which existence and uniqueness of the solution were proven [12], [46]. Denoting with $\mathbf{M}^{ij}_{\mathbf{IE}}$, $\mathbf{K}^{ij}_{\mathbf{IE}}$, and $\mathbf{C}^{ij}_{\mathbf{IE}}$ the (i, j)-th components of the infinite element mass, stiffness, and damping element matrices respectively, for the Astley-Leis formulation we have:

$$\mathbf{M}^{ij}_{\mathbf{IE}} = \frac{1}{c^2} \int_{\Omega^e} \left\{ w \boldsymbol{\psi}_i \boldsymbol{\psi}_j \left[1 - \|\nabla_x \mu\|^2 \right] \right\} \mathrm{d}\Omega, \tag{24}$$

$$\mathbf{K}^{ij}_{\mathbf{IE}} = \int_{\Omega^e} \left\{ (\boldsymbol{\psi}_i \nabla_x w + w \nabla_x \boldsymbol{\psi}_i) \cdot \nabla_x \boldsymbol{\psi}_j \right\} \mathrm{d}\Omega \tag{25}$$

$$\begin{aligned} \mathbf{C}^{ij}_{\mathbf{IE}} = \frac{1}{c} \int_{\Omega^e} \big\{ & w \boldsymbol{\psi}_i \nabla_x \mu \cdot \nabla_x \boldsymbol{\psi}_j - \boldsymbol{\psi}_i \boldsymbol{\psi}_j \nabla_x \mu \cdot \nabla_x w \\ & - w \boldsymbol{\psi}_j \nabla_x \boldsymbol{\psi}_i \cdot \nabla_x \mu \big\} \, \mathrm{d}\Omega \end{aligned} \tag{26}$$

2.3. Review of conditions for stability

In this subsection, we analyze the conditions under which the Astley-Leis formulation is stable. Astley and Hamilton [21] empirically observed that when "zero-mass" Astley-Leis infinite elements are constructed, the formulation is time-stable. Cipolla [47] argued that the positive semi-definiteness of the global mass matrix is a necessary condition for stability. Our numerical experiments, some of which are presented here, while others have been published in previous works ([36], [39], [48]) or remain unpublished, indicate that

such condition is not only necessary, but also sufficient. This assumption has been observed to hold true for a wide variety of numerical experiments, but it is not yet underpinned by any formal proof.

This analysis extends the one carried out by Astley and Hamilton [21]. In particular, in Section 3.5 of [21], only the system matrices relative to the infinite elements are considered; here, by contrast, we include the case where the interior domain is discretized with finite elements. Moreover, in Section 3.5 of [21] only the case where the inner surface of the infinite element is an arc of a circle is inspected; in this subsection, we extend the analysis to arbitrary convex shapes.

A symmetric matrix $\mathbf{A} \in \mathbb{R}^{n_\mathrm{A} \times n_\mathrm{A}}$ is defined positive semi-definite when

$$\mathbf{a}^\top \mathbf{A} \mathbf{a} \geq 0, \ \forall \mathbf{a} \in \mathbb{R}^{n_\mathrm{A}}. \tag{27}$$

For the sake of brevity, we will adopt $\mathbf{A} \geq 0$ as a shorthand notation to indicate positive semi-definiteness of the matrix $\mathbf{A}$. Because of the infinite elements' contribution, the mass matrix may not always be positive semi-definite, causing the system to become unstable.

In Appendix C.1, we prove that if the mass submatrix relative to the infinite domain $\mathbf{M_{IE}}$ is positive semi-definite, then the global mass matrix $\mathbf{M}$ is also positive semi-definite. In Appendix C.2, we show that $\mathbf{M_{IE}} \geq 0$, provided that the element mass matrix $\mathbf{M}^e_{\mathbf{IE}} \geq 0$ for all the infinite elements. In Appendix C.3, we show that $\mathbf{M}^e_{\mathbf{IE}} \geq 0$ if $\|\nabla_x \mu\| \leq 1$ for any point within the infinite element. Therefore, we can conclude that if $\|\nabla_x \mu\| \leq 1$ everywhere in the exterior domain, then $\mathbf{M} \geq 0$. As already mentioned, our empirical observations indicate that the positive semi-definiteness of the global mass matrix lead to a stable system.

In Appendix C.4 we show that, if the infinite elements are extruded orthogonally to the envelope Γ, and if the envelope is discretized exactly, $\|\nabla_x \mu\| = 1$ for any point within the infinite elements. However, because of the geometrical approximation, small numerical errors can arise, potentially causing $\|\nabla_x \mu\| > 1$ for some points in the exterior domain. Astley and Hamilton [21] proposed to remedy this effect by enforcing $\mathbf{M_{IE}} = 0$ (which is equivalent to imposing $\|\nabla_x \mu\| = 1$ everywhere in the exterior domain), arguing that the consequent change in the frequency domain solution is negligible, provided that the transverse node spacing is sufficiently fine to resolve adequately the curvature of Γ. As shown in Appendix C.1, it is actually sufficient to impose $\|\nabla_x \mu\| \leq 1$ to ensure $\mathbf{M_{IE}} \geq 0$; this can be achieved by

enforcing $\|\nabla_x \mu\| = 1$ only for points where $\|\nabla_x \mu\| > 1$ and leaving $\|\nabla_x \mu\|$ unchanged elsewhere.

In summary , we have shown in this section that if the infinite elements are extruded orthogonally and if the mass matrix correction is applied to account for geometrical discretization errors, the global mass matrix in the Astley-Leis formulation is positive semi-definite. However, requiring that the infinite elements are extruded orthogonally to Γ means that, in general, the virtual sources cannot be located at the center of radiation. This limits the accuracy of all standard mapped formulations, especially for envelopes with a high aspect ratio, and explains the need to develop a new flexible infinite element formulation.

3. Flexible infinite element formulation

In this section, we describe the new flexible formulation, for which the geometric and field shape functions are constructed using two distinct mappings. This feature makes the accuracy of our formulation independent of the location of the mapping nodes in the exterior domain. As a consequence, the flexible infinite elements can be used to accurately simulate transient acoustic wave propagation problems for arbitrarily convex-shaped envelopes.

3.1. Modified shape functions

Our objective is to develop an infinite element trial solution which mimics a truncated version of the Atkinson-Wilcox expansion, irrespective of the location of the mapping nodes. This is achieved by using r (i.e., the distance from the center of radiation) for the definition of the shape and phase functions, rather than the coordinate ξ (i.e., the interpolated distance from the virtual sources). To do so, we first redefine the phase distance as

$$\overline{\mu}(s,t,v) = r(s,t,v) - \overline{a}(s,t), \tag{28}$$

where r is computed according to (17), and $\overline{a}$ is the radial distance evaluated on Γ:

$$\overline{a}(s,t) = r(s,t,v=-1). \tag{29}$$

The symbol $\bar{\cdot}$ is used for the new variables defined in the flexible formulation. One may try to write the shape functions as

$$\boldsymbol{\Phi} = \boldsymbol{\psi}^{\boldsymbol{r}}(s,t,r(s,t,v)) \exp\left[-\mathrm{i}k\overline{\mu}\right], \tag{30}$$

where $\boldsymbol{\psi}^{\boldsymbol{r}}(s,t,r(s,t,v))$ would be obtained as a tensor product between the usual polynomial functions in the tangential direction and rational functions in the radial direction, specifically designed to satisfy (21). However, the construction of these rational functions would not be trivial, and the effort of implementing such a formulation in an existing FEM software would be substantial. Instead, we introduce a new auxiliary mapping between the radial distance r and the auxiliary coordinate $\overline{v}$:

$$\overline{v}(s,t,v) = 1 - \frac{2\overline{a}(s,t)}{r(s,t,v)}. \tag{31}$$

It should be noticed that this mapping largely resembles the inverse of mapping (12), with r, $\overline{v}$, and $\overline{a}$ instead of ξ, v, and a. The new auxiliary mapping is schematically represented in Figure 3.

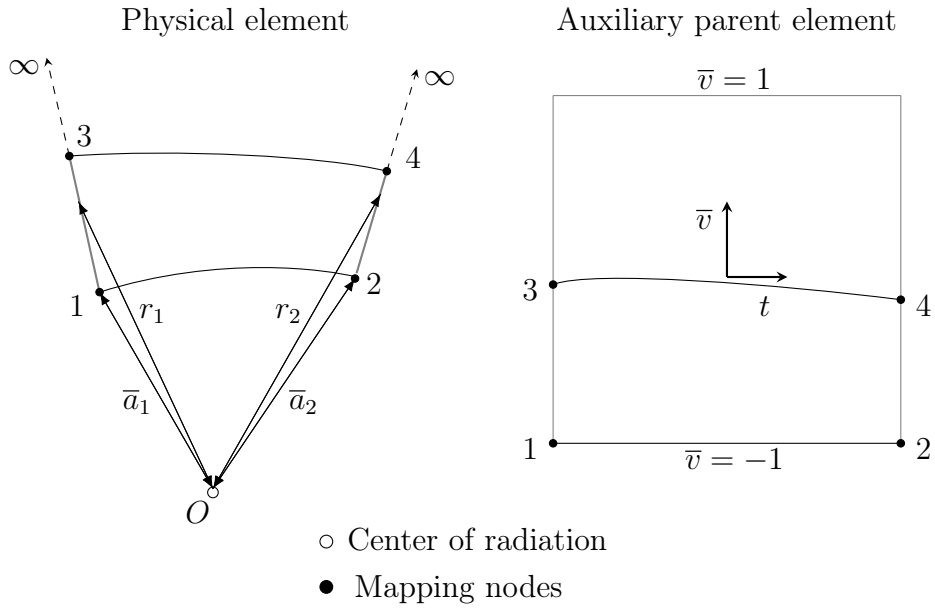

Figure 3: Schematic representation of the auxiliary mapping in a flexible infinite element

Exploiting the auxiliary mapping, we propose a new formulation for the shape functions:

$$\boldsymbol{\Phi} = \boldsymbol{\psi}(s,t,\overline{v}) \exp\left[-\mathrm{i}k\overline{\mu}\right], \tag{32}$$

where $\boldsymbol{\psi}$ are the usual polynomials, expressed with respect to the variables $s,t,\overline{v}$ instead of the variables s,t,v as in (18) for the Astley-Leis formulation.

As shown in Figure 3, $\overline{v} = -1$ on the envelope Γ, which is necessary to ensure continuity of the shape functions between the interior and the exterior domains. By inserting the radial mapping (31) in (32), it can be verified that the following holds true

$$\tilde{p} \sim \left(\frac{\alpha_1}{r} + ... + \frac{\alpha_m}{r^m}\right) \exp\left[-\mathrm{i}k(r-a)\right], \tag{33}$$

not only for points along the infinite edges but for any point inside the e-th infinite element. In other words, the trial solution within an individual mapped element reproduces a truncated version of the global Wilcox-Atkinson theorem, irrespective of the geometry of the infinite elements. Therefore, the concept of virtual sources does not apply to our formulation. This feature makes our formulation more geometrically flexible than traditional mapped formulations since the accuracy does not depend on the positioning of the mapping nodes.

The evaluation of $\nabla_x \boldsymbol{\psi}$, necessary to compute the integrals in (25) and (26), is carried out in the usual way:

$$\nabla_x \boldsymbol{\psi} = \mathbf{J} \nabla_u \boldsymbol{\psi}, \tag{34}$$

where $\mathbf{J}$ is the Jacobian of the mapping between the Cartesian coordinates (x, y, z) and the parent element coordinates (s, t, v), while $\nabla_u = \left[\frac{\partial}{\partial s}, \frac{\partial}{\partial t}, \frac{\partial}{\partial v}\right]^\top$. In standard FEM, the computation of $\nabla_u \boldsymbol{\psi}$ typically involves shape functions that depend directly on the parent element coordinates. However, in our case, $\boldsymbol{\psi}$ is a function of the auxiliary parent element coordinate $\overline{v}$, which introduces a variation in how the gradient $\nabla_u \boldsymbol{\psi}$ is computed. Nevertheless, implementing this computation in software remains straightforward. This involves leveraging existing FEM frameworks with minor modifications to accommodate the dependency on $\overline{v}$, as shown in Appendix A. As in the Astley-Leis formulation, the test functions are chosen as the weighted complex conjugate of the shape functions:

$$\widetilde{\boldsymbol{\phi}} = w \boldsymbol{\psi}(s, t, v) \exp\left[+ik\overline{\mu}\right]. \tag{35}$$

The implications of this choice were already discussed in detail in Section 2.2.2.

3.2. Time-domain stability of the flexible infinite element

The new flexible infinite element requires a separate stability analysis since the definition of $\overline{\mu}$ in (28) differs from the definition of μ in (16), used in

standard mapped formulations. In particular, even when the infinite elements are extruded orthogonally to the envelope Γ and there is no approximation in the geometrical discretization, it cannot be guaranteed that $\|\nabla_x \overline{\mu}\| \leq 1$ everywhere. This poses a challenge for the stability of the method.

In Appendix D, we analyze the behavior of $\|\nabla_x \overline{\mu}\|$, showing that, when the infinite edges are orthogonal to the envelope Γ, $\|\nabla_x \overline{\mu}\| \leq 1$ in the near-field, while $\|\nabla_x \overline{\mu}\| \geq 1$ in the intermediate and far-field. In Section 3.2.1, we present a stabilized time-domain formulation. Finally, in Section 3.2.2, exploiting the analysis in Appendix D, we propose a strategy to guarantee the accuracy of the stabilized formulation.

3.2.1. Stabilized formulation

Because of the behavior of $\|\nabla_x \overline{\mu}\|$, analyzed in Appendix D, a strategy to stabilize the flexible infinite element formulation is necessary. To stabilize the new flexible formulation, we propose to substitute the non-stabilized mass matrix $\mathbf{M}^e_{\mathbf{IE}}$ with $\widetilde{\mathbf{M}}^e_{\mathbf{IE}}$. We consider the case where the integral in (C.3) is computed using Gauss quadrature. In this case, using the notation introduced in Appendix C.3, we can write

$$\mathbf{M}^e_{\mathbf{IE}} = \boldsymbol{\psi}^\top \mathbf{D}^e \boldsymbol{\psi}. \tag{36}$$

$$\widetilde{\mathbf{M}}^e_{\mathbf{IE}} = \boldsymbol{\psi}^\top \widetilde{\mathbf{D}}^e \boldsymbol{\psi}, \tag{37}$$

where the j-th component of the stabilized diagonal matrix $\widetilde{\mathbf{D}}^e$ is defined as:

$$\begin{cases} \widetilde{\mathbf{D}}^e_{jj} = \mathbf{D}^e_{jj} & \text{if } \|\nabla_x \mu(\mathbf{g}_j)\| \leq 1 \\ \widetilde{\mathbf{D}}^e_{jj} = 0 & \text{if } \|\nabla_x \mu(\mathbf{g}_j)\| > 1. \end{cases} \tag{38}$$

This ensures that $\widetilde{\mathbf{D}}^e \geq 0$ and therefore $\widetilde{\mathbf{M}}^e_{\mathbf{IE}} \geq 0$, which was empirically observed to lead to a time-stable formulation, as discussed in Section 2.3.

3.2.2. Accuracy of the stabilized formulation

In the previous subsection, we showed how to stabilize the flexible infinite element formulation. However, the stabilization procedure may potentially affect the accuracy of the method. This comes from the fact that some of the entries in $\widetilde{\mathbf{D}}^e$ may differ substantially from the corresponding entries in $\mathbf{D}^e$, making $\widetilde{\mathbf{M}}^e_{\mathbf{IE}}$ a bad approximation of $\mathbf{M}^e_{\mathbf{IE}}$.

Exploiting relationship (D.10), which holds when the infinite edges are extruded orthogonally to the envelope Γ, we can design a strategy to ensure

the accuracy of the flexible infinite elements after the stabilization procedure by modifying the test functions. We propose to tune the power p_w in the weight factor w, as introduced in (23), to make sure that the stabilization procedure does not significantly affect the accuracy. In practice, this is achieved by controlling the relative difference between $\widetilde{\mathbf{D}}^e$ and $\mathbf{D}^e$: the smaller this difference, the smaller the accuracy loss. We recall that in the Astley-Leis formulation $p_w = 2$, but that any $p_w \geq 2$ is admissible (see discussion in Section 2.2.2). We observe that $w = 1$ at the envelope Γ ($v = -1$) and $w \to 0$ as $v \to 1$. By increasing p_w, the weighting factor can be made arbitrarily small for $v > -1$ (i.e., for points that do not lie on the envelope Γ). Let's consider the κ-th Gauss point $\mathbf{g}_\kappa$, for which $\|\nabla_x \overline{\mu}(\mathbf{g}_\kappa)\| > 1$. Since relationship (D.10) holds for orthogonally extruded infinite edges, $\mathbf{g}_\kappa$ cannot lie on the envelope Γ. The corresponding diagonal entry in the matrix $\mathbf{D}^e$ is

$$\mathbf{D}^e_{\kappa\kappa} = \frac{1}{c^2} g^w_\kappa \cdot \det \mathbf{J}_\kappa \left(1 - \|\nabla_x \overline{\mu}(\mathbf{g}_\kappa)\|^2\right) w(\mathbf{g}_\kappa), \tag{39}$$

while the corresponding entry in $\widetilde{\mathbf{D}}^e$ is

$$\widetilde{\mathbf{D}}^e_{\kappa\kappa} = 0. \tag{40}$$

We emphasize that, since relationship (D.10) holds, it is guaranteed that $w(\mathbf{g}_\kappa) < 1$ and we can impose

$$\left|\mathbf{D}^e_{\kappa\kappa} - \widetilde{\mathbf{D}}^e_{\kappa\kappa}\right| = |\mathbf{D}^e_{\kappa\kappa}| < \epsilon, \tag{41}$$

by choosing

$$w(\mathbf{g}_\kappa) < \frac{\epsilon}{\left|\frac{1}{c^2} g^w_\kappa \cdot \det \mathbf{J}_\kappa \left(1 - \|\nabla_x \overline{\mu}(\mathbf{g}_\kappa)\|^2\right)\right|}, \tag{42}$$

where ϵ is a tolerance value, set by the user. By substituting expression (23) into (42), we obtain

$$p_w > \log\left(\frac{\epsilon}{\left|\frac{1}{c^2} g^w_\kappa \cdot \det \mathbf{J}_\kappa \left(1 - \|\nabla_x \overline{\mu}(\mathbf{g}_\kappa)\|^2\right)\right|}\right) \left[\log\left(\frac{1 - v^g_\kappa}{2}\right)\right]^{-1}. \tag{43}$$

The parameter p_w is chosen constant across the whole domain to guarantee the continuity of the test functions, such that (43) is satisfied for all the infinite elements. A smaller tolerance ϵ implies a smaller difference between $\mathbf{D}^e$ and $\widetilde{\mathbf{D}}^e$ and, as a consequence, a smaller accuracy loss after the stabilization

step. We emphasize that positive semi-definitiness of the global mass matrix is guaranteed by (38), while the accuracy of the stabilized formulation is guaranteed by (43). The accuracy-preserving procedure is applicable only to configurations where the infinite edges are extruded normally to the envelope Γ, as only in these cases can an arbitrarily accurate and positive semi-definite approximation of the global mass matrix be derived. This is similar to [21], where the "zero-mass" Astley-Leis infinite elements are only accurate under such normal extrusion conditions.

The only cost of selecting $p_w > 2$ is that a higher number of Gauss points are needed to carry out the computation since the order of the polynomials to be integrated increases with p_w. Typically, for numerical acoustic simulations relying on FEM, the most computationally intensive operation is the factorization of the fully assembled matrix; for this reason, despite an increase in the computational cost of the assembly step, the total computational cost of the flexible formulation is comparable to that of the Astley-Leis formulation, for the same number of DOFs. Furthermore, the flexible infinite elements often result in a drastic decrease in the number of DOFs due to their geometric flexibility, making the simulations less computationally intensive overall, as documented in Sections 5 and 6.

3.3. Infinite elements extrusion in the normal direction

As already explained in previous sections, the infinite edges need to be extruded orthogonally to the envelope Γ to ensure that a positive semi-definite global mass matrix can be constructed without a significant accuracy loss. Unfortunately, it is not trivial to compute the normal of Γ for general convex shapes. In some cases, information about the normal vectors could be provided by CAD tools, with the drawback of requiring an additional preprocessing step. In other cases, only meshed domains are available, without a reference geometry. We solve this issue by following the procedure presented in [49]. With this approach, only a mesh of the interior domain is necessary. The required normal vectors at the mapping nodes on Γ are computed as follows:

- For a vertex, the normal vector $\mathbf{n}(s,t)$ is taken as the average of the normals of the elements touching the vertex.
- Inside quadratic elements, for a node defined in the middle of an edge (or face), $\mathbf{n}(s,t)$ is computed as the average of the normal vectors at the end nodes belonging to the edge (or face).

The user has to specify the extrusion length, which is the distance a as defined is (10), for the i-th mapping node on Γ, with parent element coordinates $(s_i, t_i, -1)$. Then, the location of the mapping node $i+n$ inside the exterior domain is determined in the following way:

$$\mathbf{x}_{i+n} = \mathbf{x}_i + a\mathbf{n}(s_i, t_i). \tag{44}$$

The process is repeated for all the mapping nodes on the envelope Γ, for all the infinite elements.

4. Software implementation of high-order finite and infinite elements

In this subsection, we discuss the implementation of the infinite elements into a high-order FEM code. The considerations made here hold for both the Astley-Leis formulation and the flexible infinite elements. We refer to the adaptive order p-FEM approach described in [50], where Lobatto shape functions (also called integrated Legendre polynomials) are used, and to [51], where the method was generalized to include anisotropic orders. For a number of Helmholtz problems, this approach has been shown to drastically improve the efficiency of the numerical models, when compared with conventional FEM, exploiting the fact that high-order polynomial approximations are more effective at controlling the pollution effect. An added benefit of using a hierarchical set of shape functions, such as the Lobatto polynomials, is found when solutions in the frequency domain are required over a range of frequencies. It is possible to compute the element matrices only once for the highest order, and then, at each frequency, one can extract only the required portion of these matrices to assemble the global matrix. A key feature of the proposed method is the use of a simple local error indicator to select a priori the polynomial order in each element. For calculations over a range of frequencies, this approach requires only a single mesh. For each frequency, the error estimator adaptively selects the suitable polynomial order in each element to meet the accuracy target.

Infinite elements based on Lagrange polynomials have been shown to present conditioning problems for high radial orders [31]. The use of Jacobi [31] and Berstein [52] polynomials has been proposed to improve the conditioning and optimize the performance of Krylov-based iterative solvers. As pointed out in [31], Lobatto polynomials, even though suboptimal from a conditioning perspective, outperform Lagrange polynomials in this respect.

By adopting the same type of polynomials for finite and infinite elements, the software implementation becomes particularly easy. In this case, the infinite element subroutine can be developed by reusing most of the routines called by its finite element counterpart. The only differences are that the new radial geometric mapping (15) needs to be implemented, and different formulas need to be used for the computation of the system matrices, which does not require any additional implementation effort. In other words, in a software implementation, the infinite elements can be simply seen as specialized anisotropic high-order elements. This is an important aspect, as the implementation burden of the infinite element method may hinder its broad use in practical applications. An additional benefit of using Lobatto polynomials in the exterior domain is that the hierarchical structure of the system matrices is preserved for unbounded-domain simulations and can be exploited for frequency-domain calculations.

The interpolation order for each element in the FE domain is selected based on the a priori error estimator described in [50]; the radial order on the infinite edges is manually selected in this work, while the orders on the envelope Γ are designed to ensure continuity with the FE domain. Future work may consider automatic order assignment for radial shape functions as well. Finally, vertex, edge and face DOFs are set to zero at infinity ($v = 1$ in the parent element) to enforce the decay of the pressure field.

5. Numerical validation

In this section, the flexible infinite element is compared to the Astley-Leis formulation, with numerical examples in two and three dimensions, both in the frequency domain and in the time domain. The FE domain is meshed with the mesh generator `Gmsh` [53], while the infinite elements are extruded at run time, using one of the following strategies:

- The confocal-rays approach, where the infinite edges are extruded in the radial direction and converge towards the center of radiation. In the Astley-Leis formulation, this means that all the virtual sources coincide with the center of radiation.

- The normal-rays approach, where the infinite edges are aligned with the vector $\mathbf{n}$, normal to the FE boundary envelope Γ.

Curved triangular or tetrahedral elements are used in the interior domain, while the exterior mesh is made of quadrangular or prismatic elements. The results are obtained using an in-house Matlab code.

In the following examples, we will often refer to the relative L^2-error between the numerical and the reference solution, p_{num} and p_{ref} respectively, computed on the envelope Γ:

$$E_2(\Gamma) = \frac{\|p_{\text{num}} - p_{\text{ref}}\|_{L^2(\Gamma)}}{\|p_{\text{ref}}\|_{L^2(\Gamma)}} \tag{45}$$

and in the interior domain Ω_i:

$$E_2(\Omega_i) = \frac{\|p_{\text{num}} - p_{\text{ref}}\|_{L^2(\Omega_i)}}{\|p_{\text{ref}}\|_{L^2(\Omega_i)}}. \tag{46}$$

When using the flexible formulation for transient problems, we will measure the error induced in the frequency domain by the stabilization procedure (see discussion in Section 3.2.2), for the largest frequency of interest, as:

$$E^{\text{st}}_{\infty}(\Omega_i) = \frac{\|p^{\text{st}}_{\text{num}} - p^{\text{unst}}_{\text{num}}\|_{\infty(\Omega_i)}}{\|p^{\text{unst}}_{\text{num}}\|_{\infty(\Omega_i)}}, \tag{47}$$

where $p^{\text{st}}_{\text{num}}$ is obtained using the stabilized formulation, while $p^{\text{unst}}_{\text{num}}$ is obtained using the non-stabilized formulation. The subscript ∞ indicates the $\infty-$norm, computed for a generic vector $\mathbf{v}$ as: $||\mathbf{v}||_\infty = \max_i |v_i|$.

5.1. Monopole source in 2D

First, we analyze the case of a monopole source in a 2D domain. Considering a monopole source located at the center of radiation, we have the following inhomogeneous Helmholtz equation in the unbounded domain Ω:

$$\nabla^2 p + k^2 p = A\delta(r) \quad \text{ in } \Omega, \tag{48}$$

where A is the source strength. The reference acoustic pressure amplitude p_{ref}, which is the analytical solution to Eq. (48), is given by:

$$p_{\text{ref}}(r) = \mathrm{i}\frac{A}{4} H_0^{(2)}(kr), \tag{49}$$

where $H_0^{(2)}$ is the zeroth order Hankel function of the second kind. The source is enclosed by a convex envelope, and the two meshes generated using the

confocal-rays and the normal-rays approach are shown in Figure 4. A node is placed at the source point. In its vicinity, the mesh is refined due to the singularity of the analytical solution at $r = 0$, while in the rest of the domain larger elements are used to fully exploit the efficiency of high-order FEM. The characteristic dimension of the geometry is $L = 2$ The characteristic length of the elements at the interface between the interior domain and the exterior domain is $h = 0.25$.

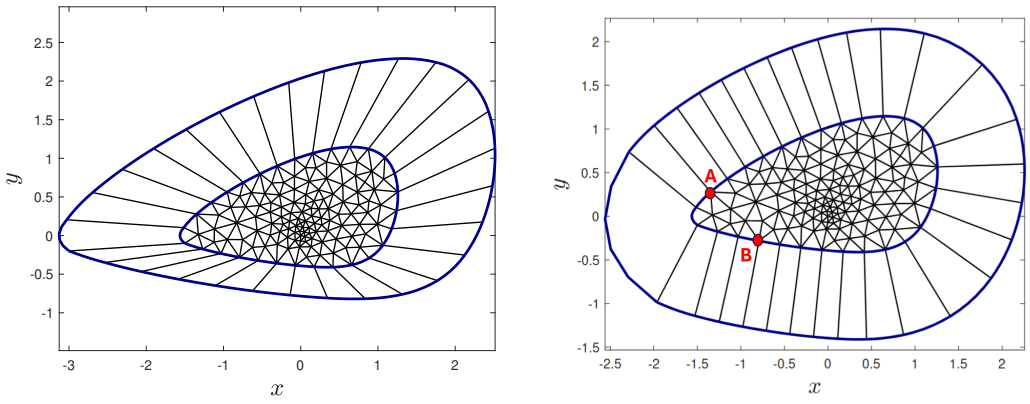

(a) Confocal rays (b) Normal rays

Figure 4: 2D meshes used for the numerical experiments. The FEM mesh, the envelopes Γ and Υ (in blue) and the portion of the infinite edges between Γ and Υ are shown. In the confocal-rays approach, all the virtual sources coincide with the center of radiation. In the normal-rays approach, all the infinite edges are locally orthogonal to the envelope Γ. In both cases, the mesh is refined in the vicinity of the monopole source location, which coincides with the center of radiation.

5.1.1. Frequency-domain results

The frequency-domain solutions presented herein are computed using a uniform interpolation order throughout the entire computational domain, i.e., the order of interpolation is identical for all finite elements and infinite elements in all directions. Numerical convergence studies are done by investigating the effect of the order chosen on the accuracy of the methods. First of all, we compare the performance of the new flexible infinite element against the Astley-Leis formulation, for the confocal-rays configuration. Even though, for the configuration considered, all the virtual sources coincide with the center of radiation, the Astley-Leis formulation and the flexible formulation are still different. This is because, for the Astley-Leis

formulation, the radial coordinates are found, as specified in (12) and (13), using the standard interpolating functions, while, for the flexible infinite element, they are computed as a function of the Cartesian coordinates, using (17) and (29). In Figure 5 we plot the L^2-error on the envelope Γ for several frequencies, for both approaches, as a function of the interpolation order. For all four frequencies, the L^2-error of the standard Astely-Leis formula-

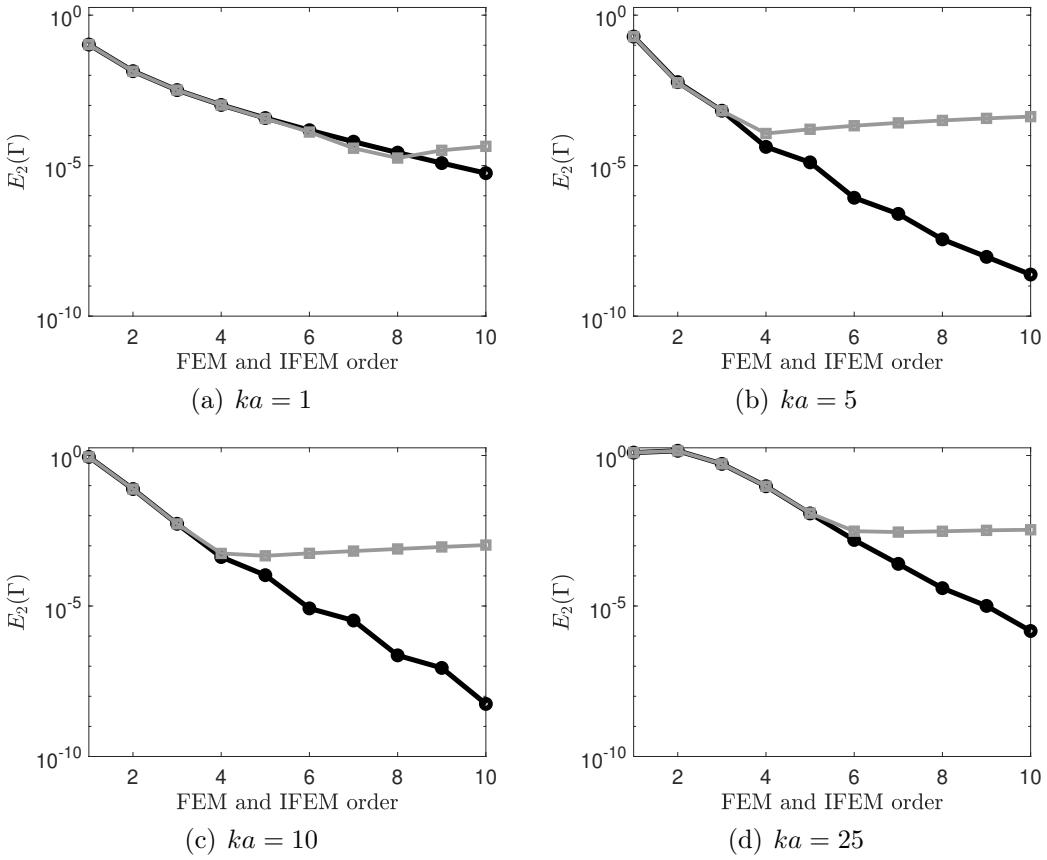

(a) $ka = 1$ (b) $ka = 5$

(c) $ka = 10$ (d) $ka = 25$

Figure 5: Flexible infinite element (black) vs standard Astley-Leis element (gray), results for the confocal-rays configuration. All the virtual sources coincide with the center of radiation and with the location of the physical source.

tion reaches a plateau, while the flexible infinite element approach displays better p-convergence properties. These results are explained by the fact that (33) is satisfied everywhere for the flexible infinite elements, while for the Astley-Leis formulation it is only valid along the infinite edges when the

confocal-rays extrusion approach is adopted (see discussion in Appendix B). In other words, the trial solution mimics the truncated multipole expansion (9) in the whole exterior domain for the flexible formulation, but only along the infinite edges for the Astley-Leis formulation. The resulting accuracy difference is higher for coarser meshes, which are typically used in the context of high-order adaptive FEM, while it is negligible when fine meshes are used.

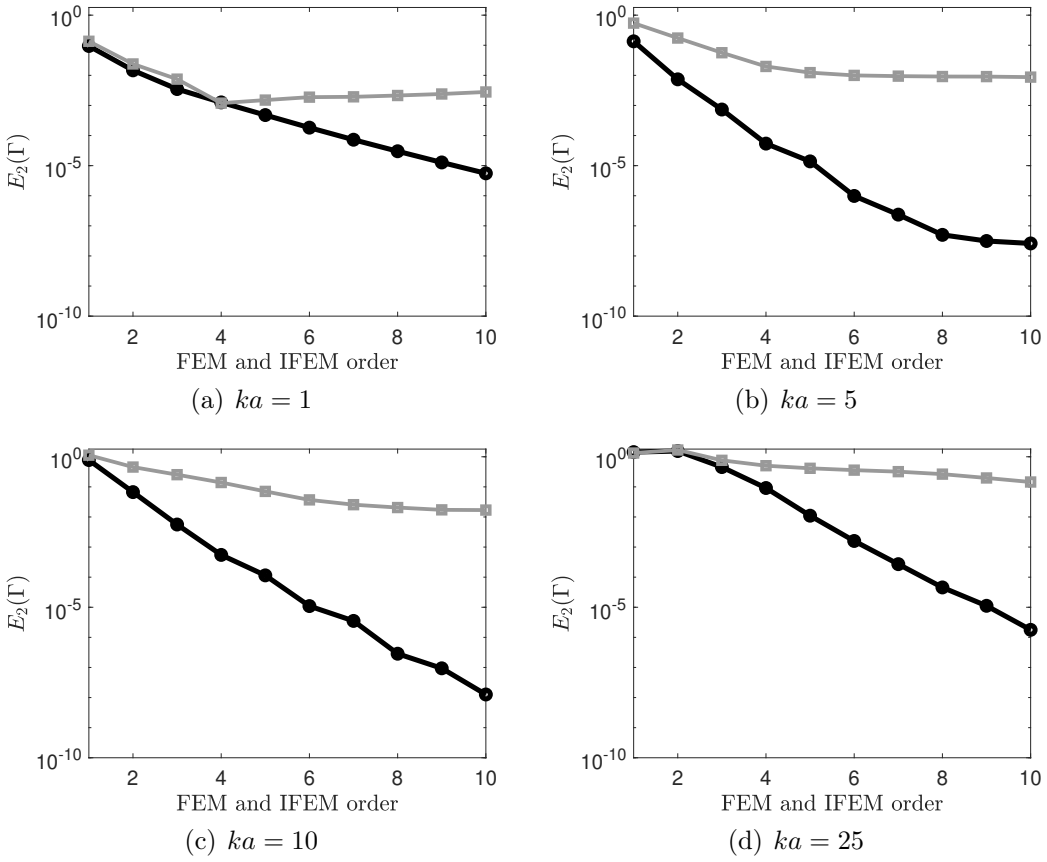

(a) $ka = 1$ (b) $ka = 5$

(c) $ka = 10$ (d) $ka = 25$

Figure 6: Flexible infinite element (black) vs standard Astley-Leis element (gray), results for the normal-rays configuration. The mesh extrusion is performed as described in Section 3.3.

Next, we compare the flexible infinite elements with the Astley-Leis infinite elements when the normal-rays extrusion strategy is adopted. This serves as a preliminary to the time-domain comparison, where the normal rays strategy is the only one capable of delivering stable and accurate re-

sults. In Figure 6, we present evidence of the significant accuracy enhancement achieved through the flexible formulation. In this case, the results are explained by the fact that, once again, (33) is satisfied everywhere for the flexible formulation since the space spanned by the shape functions does not depend on the orientation of the infinite elements; for the Astley-Leis infinite elements, by contrast, (33) is not satisfied since the virtual sources do not coincide with the center of radiation.

5.1.2. Time domain

As discussed in 2.3, empirical evidence suggests that when the infinite element mass matrix is not positive definite, the system is prone to instability. The confocal-rays extrusion approach typically results in a mass matrix that cannot be accurately approximated by a positive semi-definite matrix in either the Astley-Leis or flexible formulations. For this reason, we focus only on the normal-rays approach. For this example, the monopole source is placed at $(0.5, 0.4)$ to show that the flexible infinite elements work well even when the center of radiation does not coincide with the physical source. The source is located at a node point. The input signal used for the simulation is a sine-wave, with $ka = 20$, filtered using the Hamming window. So, the forcing vector $\mathbf{f}_{\boldsymbol{\tau}}(\tau)$, with $\tau \in [0, T]$, is

$$\mathbf{f}_{\boldsymbol{\tau}}(\tau) = \underbrace{\frac{25}{46}\left[1 - \cos\left(\frac{2\pi\tau}{T}\right)\right]}_{\text{Hamming window}} \sin(k\tau)\mathbf{f}, \tag{50}$$

where $\mathbf{f} \in \mathbb{R}^{n_{\text{DOF}}}$ is the forcing vector in the frequency domain, i.e., the right-hand side in Eq. (7). The polynomial order for each element in the interior domain is selected adaptively, using the a priori error indicator from Bériot et al. [50], with target L^2-error $E_2 = 0.01$, while the radial order in the infinite domain is set to $m = 6$ for both cases. The power in (23) for the flexible formulation is set to $p_w = 6$ and the maximum relative error induced by the stabilization procedure is $E_\infty^{\text{st}} = 0.0007$, computed according to (47) for the frequency range considered. In other words, it is clear that the error induced by the stabilization procedure is negligible since it is largely below the target error used to select the orders in the FEM domain.

By solving the quadratic eigenvalue problem

$$\left[\lambda^2\mathbf{M} + \lambda\mathbf{C} + \mathbf{K}\right]\mathbf{p}_\lambda = 0, \tag{51}$$

we verify that all the eigenvalues λ have real part smaller than zero, which confirms that the flexible stabilized and the "zero-mass" Astley-Leis formulations are indeed stable.

A reference analytical solution is obtained by first computing the inverse Laplace transform of the frequency-domain solution given in (49) to derive the system's impulse response, and then convolving this impulse response with the input signal defined in (50) to determine the system's time-domain response.

In Figure 7, we plot the non-dimensional acoustic pressure ($= p/\rho c^2$) for two points on the convex envelope (point A $= (-1.3, 0.2)$ and point B $= (-0.78, -0.24)$) as a function of non-dimensional time ($= c\tau/a$) for the "zero-mass" Astley-Leis formulation and the stabilized flexible formulation, together with the reference solution. The numerical solution obtained using the flexible formulation closely matches the reference solution, while the Astley-Leis formulation does not provide satisfactory results, as expected, due to the non-circular interior domain.

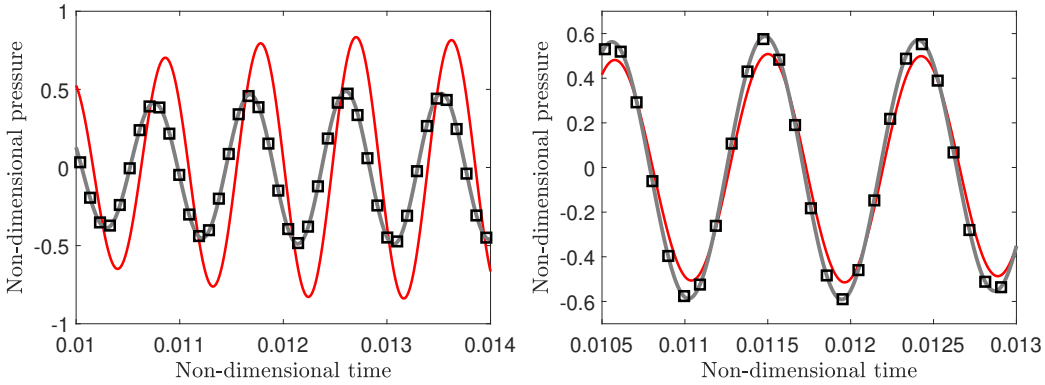

(a) Point A = (-1.3, 0.2). (b) Point B = (-0.78, -0.24).

Figure 7: Performance of the stabilized flexible and "zero-mass" Astley-Leis formulation for an arbitrary convex envelope (see Figure 4), in the time domain, using the normal-rays extrusion strategy. Pressure history at points A and B on the convex envelope Γ. Comparison between reference (gray line), stabilized flexible infinite element (black squares) and "zero-mass" Astley-Leis formulation (red line). The radial order in the exterior domain is set to $m = 6$, while the order in the interior domain is determined through the a priori error estimator.

5.2. Scattering of a plane wave by a sphere

In this subsection, we consider the scattering of a plane wave by a sphere, and we test the performance of the flexible infinite elements and of the Astley-Leis infinite elements. Several polyhedral shapes with rounded edges were used as enclosing surfaces. Rounding the corners is necessary to guarantee the accuracy of the method, regardless of the infinite element formulation used, since the normal vector has to be continuous throughout the whole surface for the extrusion direction to be orthogonal to the envelope at any point.

The scattering sphere has unit radius $a = 1$, while the pseudo-polyhedral domains have a midradius of 2 and a fillet radius of 0.2. The mesh used in the interior domain has elements with a characteristic length $h = 0.3$, with a refinement corresponding to the rounded corners to resolve the geometric details. The orders in the FEM region are once again set adaptively, using the a priori error indicator from Bériot et al. [50], with target L^2-error $E_2 = 0.01$.

5.2.1. Frequency-domain results

We consider an incident plane wave travelling in the $x-$direction, and we solve for the scattered component of the acoustic field. The acoustic pressure amplitude of the scattered field for this problem is given by:

$$p_{\text{ref}}(\mathbf{x}) = -\sum_{m=0}^{\infty} \mathrm{i}^m (2m+1) \frac{j_m'(ka)}{H_m^{(2)\prime}(ka)} H_m^{(2)}(kr) P_m(x/r), \quad r \geq a, \tag{52}$$

where j_m is the m-th order spherical Bessel function, $H_m^{(2)}$ is the m-th order second-kind spherical Hankel function, and P_m is the m-th order Legendre polynomial. The numerical simulation is set up by enforcing a Neumann boundary condition on the sphere. This condition specifies that the normal derivative of the numerical solution on the boundary must match the negative normal derivative of the incident solution.

The best-interpolation error is computed as the relative L^2-error between the analytical solution and its L^2-projection onto the finite element space:

$$\mathbf{E}_{\text{Best}} = \frac{\|\mathcal{P} p_{\text{ref}} - p_{\text{ref}}\|_{L^2(\Omega_i)}}{\|p_{\text{ref}}\|_{L^2(\Omega_i)}}. \tag{53}$$

This error corresponds to the best numerical solution that can be reached, given the FE mesh and the orders used, irrespective of the infinite element

formulation used. In Figure 8 we show the numerical results obtained using flexible infinite elements extruded in the normal direction. We conducted numerous simulations, varying the radial order m in the exterior domain from 1 to 10. It can be observed that for the flexible formulation the relative L^2-error in the interior domain $E_2(\Omega_i)$ approaches the best interpolation error for increasing radial order m. The pseudo-tetrahedron is the most challenging shape since, in this case, the envelope Γ is closer to the scattering surface. These results support the method's applicability and accuracy in a three-dimensional setting. As expected, the Astley-Leis formulation results in larger errors and slower convergence, especially at high frequencies.

5.2.2. Time-domain results

In this subsection, out of all the pseudo-polyhedral shapes presented in Section 5.2.1, only the most challenging one, the pseudo-tetrahedron, is considered. We analyze the results of a transient simulation, where the input signal is a sine-wave with $ka = 10$, filtered by the Hamming function, as in the 2D case. In Figure 9, the pressure results at the envelope points A and B for the stabilized flexible infinite elements and the "zero-mass" Astley-Leis infinite elements are shown; for both cases, the radial order in the infinite elements is set to $m = 5$. The power in (23) for the flexible formulation is set to $p_w = 6$ and the maximum relative error induced by the stabilization procedure is $E_\infty^{\text{st}} = 0.001$. Once again, the error induced by the stabilization procedure is negligible since it is largely below the target error used to select the orders in the FEM domain. A quadratic eigenvalue analysis confirms that all eigenvalues have real part smaller than zero for both formulations.

The reference numerical solution is computed on a larger FEM domain, consisting of a sphere with radius 2 surrounding the scatterer, using the "zero-mass" Astley-Leis infinite elements with the infinite edges extruded in the radial direction, such that all the virtual sources coincide with the center of the scattering sphere. The radial order in the infinite domain for the reference solution is set to $m = 10$ and the radial quantities are computed according to expressions (17) and (29). Good accuracy of the reference numerical model is guaranteed by the use of a large FEM domain, high radial order m and the modified interpolation of radial quantities, combined with the fact that all the virtual sources coincide with the center of radiation.

Also in this case, it can be noticed that the flexible formulation outperforms the traditional Astley-Leis formulation, in terms of accuracy.

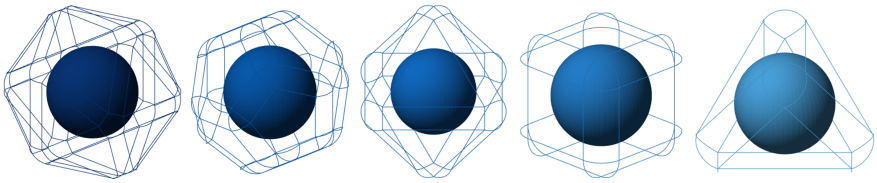

(a) Geometries.

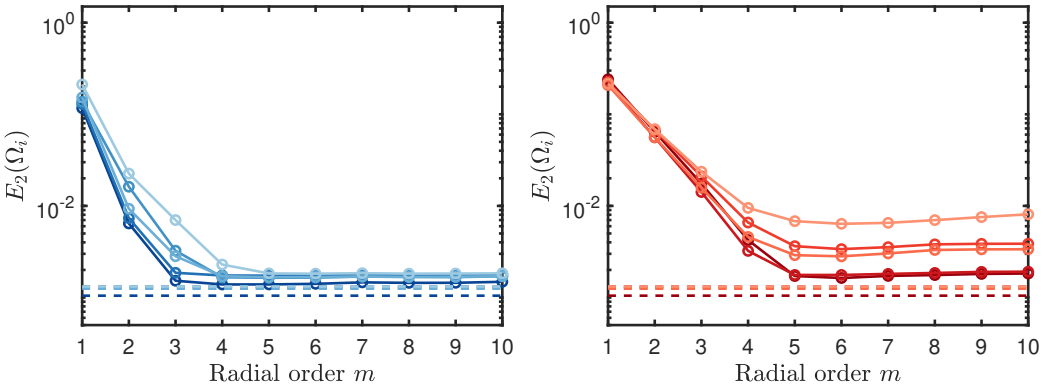

(b) $ka = 1$ (c) $ka = 1$

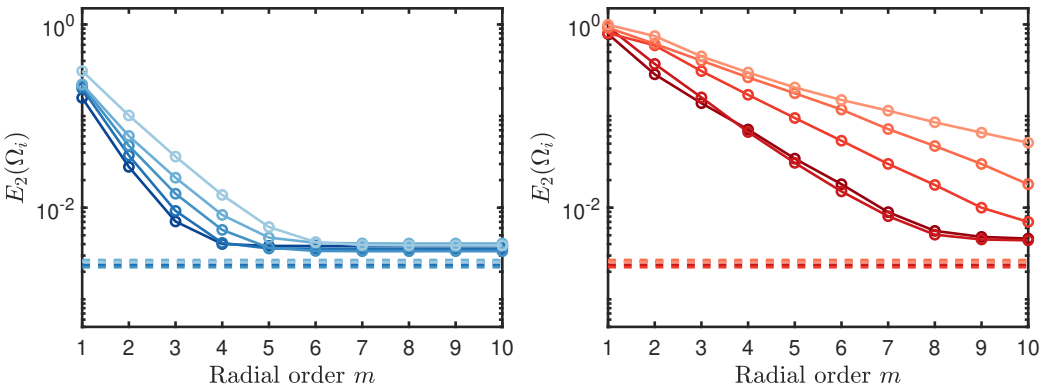

(d) $ka = 10$ (e) $ka = 10$

Figure 8: Each colored line corresponds to one pseudo-polyhedral domain. Darker colors correspond to pseudo-polyhedra with more edges. Flexible infinite elements (blue lines) vs Astley-Leis infinite elements (red lines). Dashed lines: best interpolation error in the FE domain. The interpolation order in each element of the interior domain is set adaptively, using the a priori error estimator. The radial order m is uniform throughout the exterior domain.

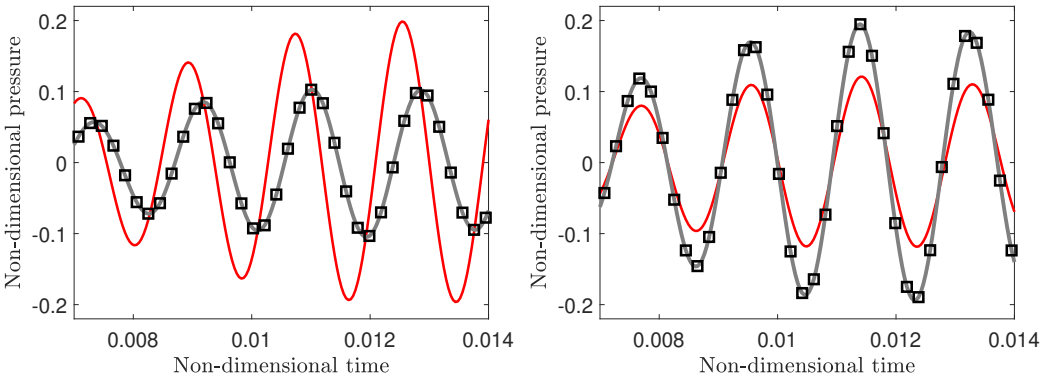

(a) Point A = (1.137, 1.222, 0.560). (b) Point B = (0.522, 1.426, 0.642).

Figure 9: Performance of the stabilized flexible formulation and "zero-mass" Astley-Leis formulation for a pseudo-tetrahedron enclosing the scattering sphere, in the time domain, using the normal-rays extrusion strategy. Pressure history at points A and B on the convex envelope Γ. Comparison between reference (gray line), flexible infinite element (black squares) and traditional Astley- Leis formulation (red line). The radial order in the exterior domain is set to $m = 6$, while the orders in the interior domain are determined through the a priori error estimator.

6. Application to a problem of industrial complexity

In this section, we present a procedure to tackle unbounded problems of industrial complexity, using the flexible infinite element formulation. In particular, to showcase the effectiveness of the method, we consider the shark submarine, shown in Figure 10. For the frequency-domain validation, we analyze the scattering of a plane wave, while for the time domain, we consider a monopole source, located close to the FE boundary. An automatic algorithm for the creation of a convex envelope around the scatterer, together with the automatic extrusion of the infinite edges in the normal direction, is used.

To accelerate transient simulations, we use a MOR procedure, introduced by van de Walle [37] and van Ophem [38], called Automatic Krylov Subspace Algorithm (AKSA). The high level of automation of the proposed procedure, together with the computational efficiency enabled by the use of general-shaped convex envelopes, make it very attractive for realistic transient applications.

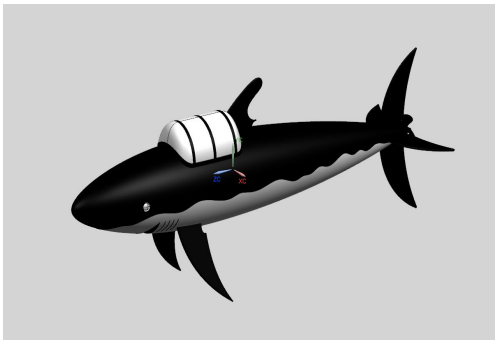

(a) CAD model.

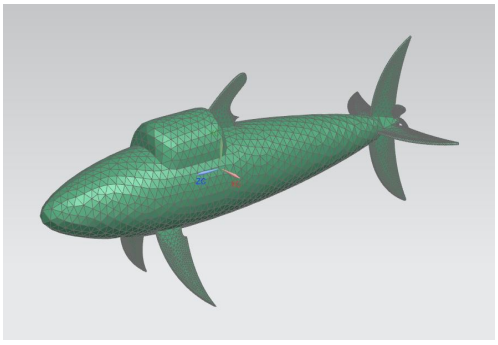

(b) Surface mesh, characteristic length $h = 0.02$.

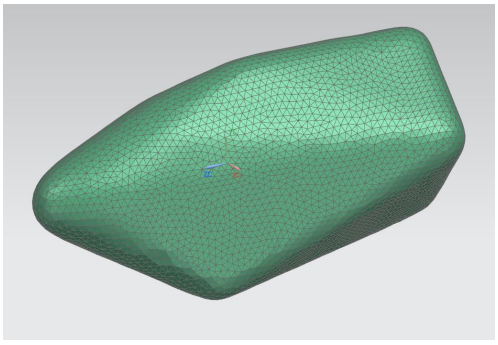

(c) Convex envelope automatically generated at the minimal distance $d = 0.05$.

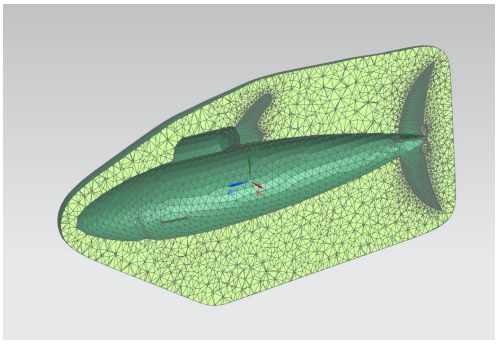

(d) Cut view of the final tetrahedral mesh.

Figure 10: Shark model.

6.1. Automatic generation of a convex domain

In this subsection, we describe the automatic process to get a mesh for the computational domain. First, a surface mesh made of second-order triangular elements, with characteristic length $h = 0.02$, is created on the submarine, which is of unit total length a. Secondly, an approximate convex hull is generated automatically using the quickhull algorithm [40], implemented in the simulation package `Simcenter 3D` [54] developed by Siemens Industry Software. The minimal distance between the submarine surface and the convex envelope is $d = 0.05$. Once again, second-order triangular elements with characteristic length $h = 0.02$ are used to mesh the external surface. Then, a volume mesh, that comprises tetrahedral second-order elements, is created between the two surface meshes. The infinite elements are extruded

automatically along the normal direction, so that the transient formulation is time-stable, following the process described in Section 3.3. The final mesh, shown in Figure 10, is made of 183 519 elements and 232 959 nodes. Since the convex envelope lies inside the smallest sphere circumscribing the scatterer, convergence is not theoretically guaranteed by the Atkinson-Wilcox theorem. In Section 6.3.1 and Section 6.3.2, we will show that, in practice, when attaching flexible infinite elements to the convex hull, good accuracy can be reached both in the time domain and in the frequency domain.

6.2. Model Order reduction procedure

Since the flexible infinite elements, as the traditional Astley-Leis infinite elements, result in frequency-independent and sparse system matrices, their use in combination with Krylov-based MOR is particularly attractive. To accelerate transient simulations, we use AKSA [37], [38], which aims at automatically building a ROM whose frequency response function (FRF) matches the FRF of the initial FOM, within a user-specified tolerance, in the frequency range of interest, by only using a few system solves and enriching the projection basis with higher-order moments. To obtain a time-domain ROM of the shark submarine, for example, valid between $ka = 5$ and $ka = 50$, with a relative error tolerance $\text{tol} = 0.01$, only 5 full system solves are necessary.

6.3. Results

6.3.1. Frequency-domain results

We now present numerical tests showcasing the accuracy of the flexible infinite element formulation for simulating the scattering of plane waves in the frequency domain. The simulations were performed for four plane waves traveling at different angles of incidence α and θ. As a reference, we use the results obtained using the automatic perfectly matched layer (AML) implementation [49], with 5 layers. The AML formulation is a well-established conformal PML technique to enforce non-reflecting conditions for acoustic simulations in the frequency domain, implemented in `Simcenter 3D`. The accuracy of the AML to simulate the scattering of plane waves from the submarine model was established in [49] through a convergence study.

For the configuration using infinite elements, the orders in the FEM domain are assigned adaptively, using the a priori error estimator from Bériot et al. [50], with target L^2-error $E_2 = 0.01$, while the radial order in the exterior domain is user-defined; for the AML case, the orders are assigned adaptively in the whole computational domain. For all cases analyzed, the

mesh used is the one shown in Figure 10. The relative L^2-error on the convex envelope is shown in Figure 11, for $ka = 10$ and $ka = 100$. In all cases, the infinite elements display good convergence, with a relative L^2-error consistently below 0.03 for radial order 8, approaching the target error.

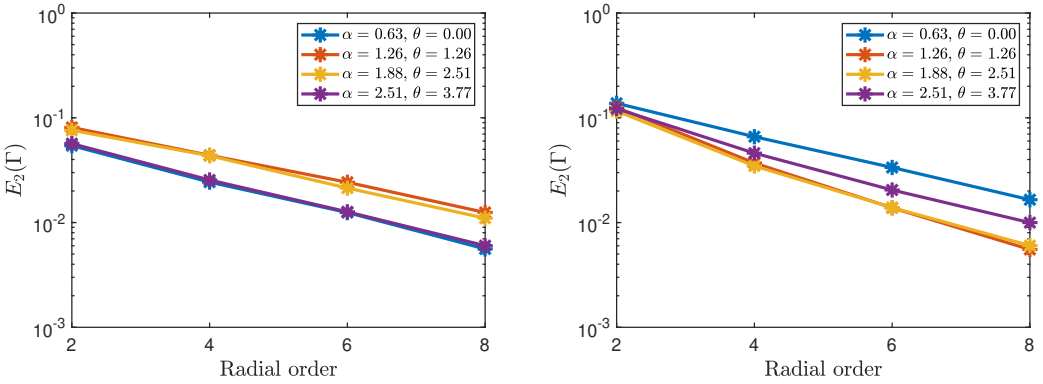

(a) $ka = 10$. (b) $ka = 100$.

Figure 11: Frequency domain results for plane waves hitting the shark submarine at different spherical angles α and θ (expressed in radians). Performance of the flexible infinite element formulation with infinite edges extruded in the normal direction. The AML implementation is used to compute the reference solution.

6.3.2. Time-domain results

Finally, we consider the scattering of a monopole source placed in front of the shark, at $(0, 0, 0.5)$.

The target L^2-error, used to compute the orders in the FEM domain, is set once again to $E_2 = 0.01$. The radial order for the infinite elements is set to $m = 8$. The power in (23) for the flexible formulation is set to $p_w = 8$ and the maximum relative error induced by the stabilization procedure is $E_\infty^{\text{st}} = 0.0002$. Once again, the error induced by the stabilization procedure is negligible when compared to the finite element discretization error.

The input signal consists of a sine wave with $ka = 45$, filtered using the Hamming window. A ROM, valid between $ka = 5$ and $ka = 50$, with a relative error tolerance tol $= 0.01$, is generated using AKSA. The FRFs of the FOM and the ROM are compared in Figure 12 for a random entry in the solution vector. The final ROM has 90 DOFs, while the initial FOM had 465 905 DOFs. We ran all our numerical experiments on a Dell desktop

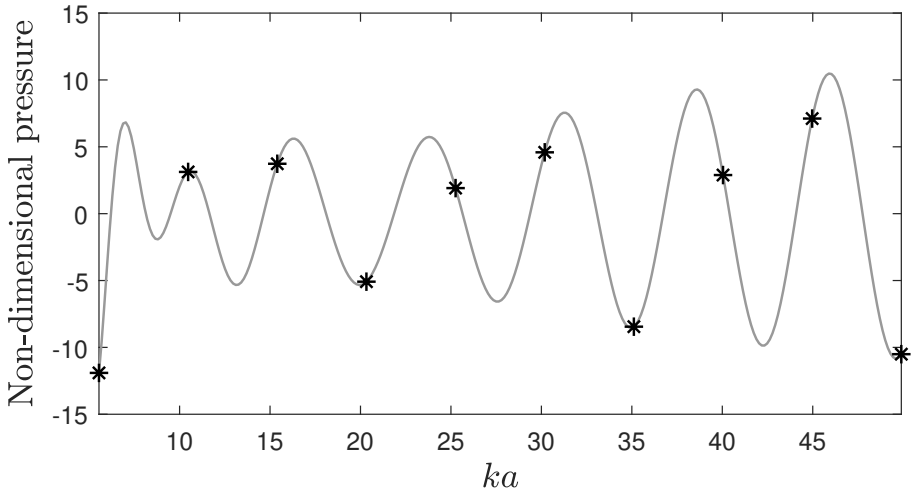

Figure 12: FRF comparison ROM (gray line) vs FOM (black stars), for a random entry in the solution vector. Results obtained by attaching flexible infinite elements to the convex hull.

computer with 384 Gb of RAM and 3.00GHz clock speed. The offline MOR procedure took 5 minutes and 45 seconds, and a single full-system solve, an operation performed several times during AKSA, required 15.5 Gb of memory.

As a reference, we compute the transient response to the same excitation using the standard Astley-Leis formulation with a spherical envelope surrounding the submarine. In this case, the model has 1 039 249 nodes, 801 405 elements and 2 515 697 DOFs, 5 times more than the convex-hull model. In this case, the offline MOR procedure takes 95 minutes, and for a full-system solve 151.9 Gb of memory are necessary. Additionally, the projection basis, which needs to be stored throughout the whole MOR process, is 5 times larger than in the previous case, as the number of rows corresponds to the DOFs of the FOM. Once again, the final ROM has 90 DOFs.

In Table 1 we summarize the data on the computational requirements to build a ROM using AKSA for the two models. This comparison highlights the computational efficiency enabled by the geometrical flexibility of the novel formulation.

In Figure 13 we plot the pressure as a function of time at different points on the submarine surface for the convex hull and the spherical envelope models. The use of the convex hull model, made possible by the newly

	DOFs	Time [min.]	Memory (full-system solve) [Gb]
Convex hull	465905	5.45	15.5
Sphere	2515697	95	151.9

Table 1: Computational requirements for AKSA, comparison between the models with convex hull and spherical envelope enclosing the submarine.

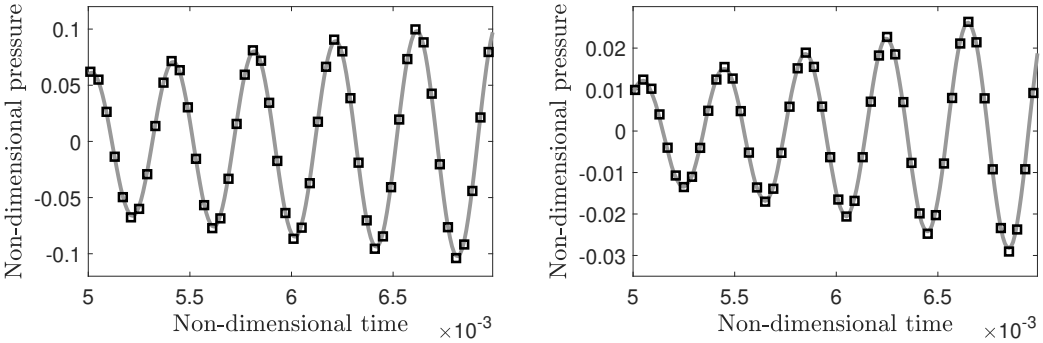

(a) Point A = (-0.116, -0.230, -0.396). (b) Point B = (-0.035, -0.002, -0.990).

Figure 13: Pressure history at points A and B on the submarine surface, using "zero-mass" Astley-Leis infinite elements attached to the spherical envelope (gray line) and stabilized flexible infinite elements attached to the convex hull (black squares).

developed flexible infinite element formulation, is clearly more efficient, since the MOR process is considerably less expensive while accuracy is preserved. In Figure 14 we show the pressure results at different time steps.

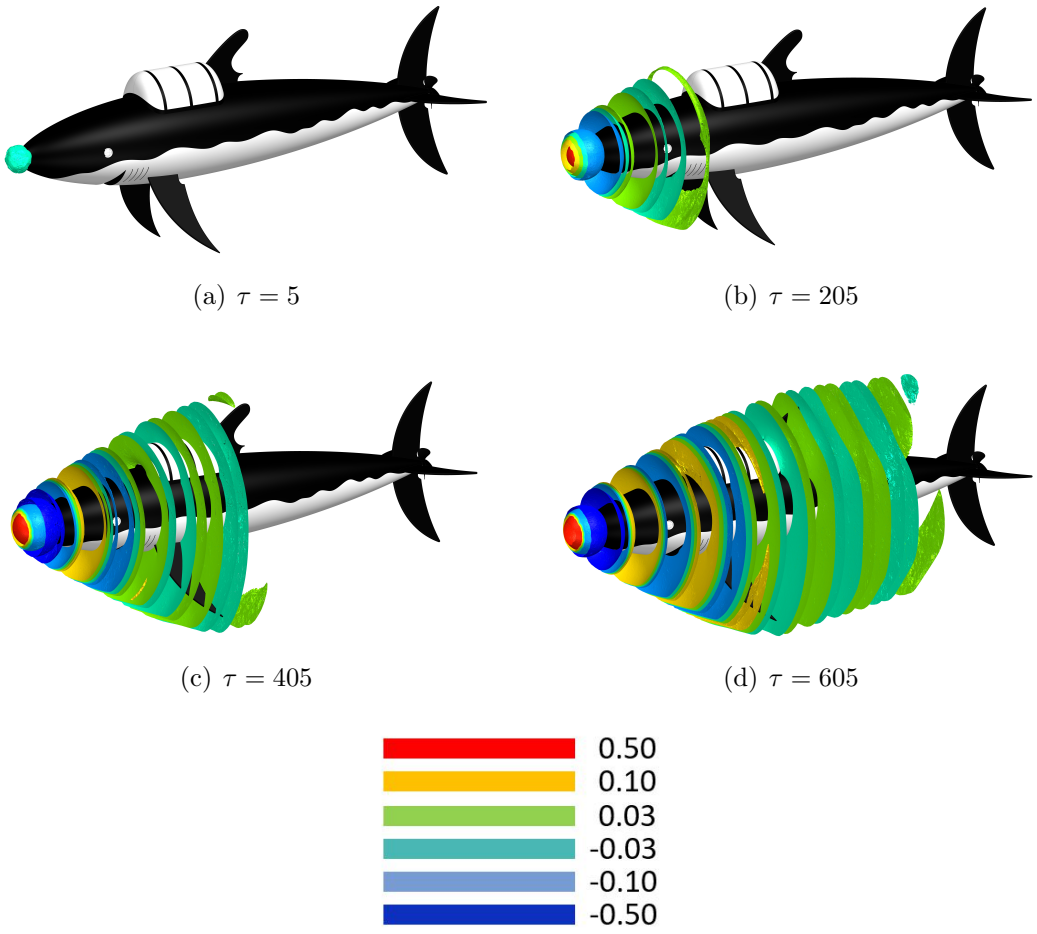

(a) $\tau = 5$

(b) $\tau = 205$

(c) $\tau = 405$

(d) $\tau = 605$

(e) Legend.

Figure 14: Transient results (non-dimensional pressure) at four different time steps, visualized in `Simcenter 3D`. Monopole source placed in front of the shark.

7. Conclusion

In this work, we introduced a novel flexible infinite element formulation for the simulation of unbounded wave propagation problems. One of the main disadvantages of traditional mapped formulations is that their accuracy depends on the geometrical configuration of the infinite elements. For transient simulations, where the infinite elements have to be extruded orthogonally to the boundary of the finite element domain, the user is not free

to place the virtual sources where desired. This limits the accuracy of such formulations, especially in the case of high-aspect-ratio acoustic domains.

In the flexible formulation, a new set of shape functions is defined, that makes the accuracy independent of the location of the mapping nodes. A stabilization procedure was derived for arbitrarily shaped convex domains. In particular, we demonstrated empirically that the flexible formulation lead to stable transient solutions when the infinite element mass matrix is positive semi-definite, or can be approximated as such without compromising the accuracy. Several 2D and 3D numerical tests were analyzed, establishing the superior accuracy of the flexible formulation compared to standard mapped infinite elements both in the frequency and in the time domains, for comparable computational cost.

The flexible infinite element formulation, and its stabilized form, were combined with a Model Order Reduction scheme to provide highly efficient frequency-domain and transient numerical models for an industrial-scale problem. The flexible formulation led to substantial computational gains by enabling the use of a non-spherical domain to enclose the complex-shaped scattering body.

Future research directions include developing an error estimator to automatically determine the radial order of the shape functions and investigating strategies to automate the choice of the power in the Astley-Leis weighting factor based on user-defined accuracy requirements. Additionally, the flexible formulation could be extended to the case with mean flow, making it applicable to aero-acoustic problems.

8. Acknowledgements

Funding: This work was supported by the Flanders Innovation & Entrepreneurship Agency (VLAIO) (grant number HBC.2020.2846). The authors are grateful to the editor Prof. J. Astley for his insightful comments and suggestions, which significantly improved the quality of the manuscript.

Appendix A. Computation of gradients in the flexible formulation

In the following we show how to compute $\nabla_u \boldsymbol{\psi}$. Given that $\boldsymbol{\psi} = \boldsymbol{\psi}(s, t, \overline{v})$, we have:

$$\frac{\partial \boldsymbol{\psi}}{\partial s} = \frac{\partial \boldsymbol{\psi}}{\partial s}\Big|_{\overline{v}} + \frac{\partial \boldsymbol{\psi}}{\partial \overline{v}} \frac{\partial \overline{v}}{\partial s}, \tag{A.1}$$

$$\frac{\partial \boldsymbol{\psi}}{\partial t} = \frac{\partial \boldsymbol{\psi}}{\partial t}\Big|_{\overline{v}} + \frac{\partial \boldsymbol{\psi}}{\partial \overline{v}} \frac{\partial \overline{v}}{\partial t}, \tag{A.2}$$

$$\frac{\partial \boldsymbol{\psi}}{\partial v} = \frac{\partial \boldsymbol{\psi}}{\partial \overline{v}} \frac{\partial \overline{v}}{\partial v}, \tag{A.3}$$

where

$$\frac{\partial \boldsymbol{\psi}}{\partial s}\Big|_{\overline{v}}, \frac{\partial \boldsymbol{\psi}}{\partial t}\Big|_{\overline{v}}, \text{ and } \frac{\partial \boldsymbol{\psi}}{\partial \overline{v}}$$

are readily available from standard FEM subroutines. In the following, we show how to compute $\nabla_u \overline{v}$. Eq. (17) can be rewritten as

$$r(s,t,v) = ||\mathbf{x}(s,t,v) \cdot \mathbf{x}(s,t,v)||. \tag{A.4}$$

Therefore we have

$$\nabla_u r = \frac{1}{r} \mathbf{x}^\top \nabla_u \mathbf{x}, \tag{A.5}$$

with $\nabla_u \mathbf{x}$ computed in the usual way. Similarly, we have:

$$\frac{\partial \overline{a}}{\partial s} = \frac{1}{\overline{a}} \mathbf{x}\Big|_{v=-1} \cdot \frac{\partial \mathbf{x}}{\partial s}\Big|_{v=-1}, \tag{A.6}$$

$$\frac{\partial \overline{a}}{\partial t} = \frac{1}{\overline{a}} \mathbf{x}\Big|_{v=-1} \cdot \frac{\partial \mathbf{x}}{\partial t}\Big|_{v=-1}. \tag{A.7}$$

Finally, from (31) follows:

$$\frac{\partial \overline{v}}{\partial s} = \frac{2}{r} \left(-\frac{\partial \overline{a}}{\partial s} + \frac{\overline{a}}{r} \frac{\partial r}{\partial s} \right), \tag{A.8}$$

$$\frac{\partial \overline{v}}{t} = \frac{2}{r} \left(-\frac{\partial \overline{a}}{\partial t} + \frac{\overline{a}}{r} \frac{\partial r}{\partial s} \right), \tag{A.9}$$

and

$$\frac{\partial \overline{v}}{\partial v} = \frac{2\overline{a}}{r^2} \frac{\partial r}{\partial v}. \tag{A.10}$$

From a software implementation perspective, these operations are straightforward to implement, as all the necessary components for the computations are already available in standard FEM. Similar considerations hold true for the derivatives of $\overline{\mu}$.

Appendix B. Interpolation of radial coordinates in the Astley-Leis formulation

Inside the e-th infinite element, we have, in general:

$$\xi \neq r, \tag{B.1}$$

even when all the virtual sources coincide with the center of radiation. This discrepancy arises because while ξ is determined using interpolating functions identical to those used to derive the Cartesian coordinates vector $\mathbf{x}$, the radial distance r cannot be obtained, in general, as a linear combination of the Cartesian coordinates.

Consider, as an example, an infinite element for which the inner surface is a circular arc, discretized with linear elements, as depicted in Figure B.15. Both virtual sources, relative to nodes 1 and 2, coincide with the center of the arc. This means that the radial distance a_1 between node 1 and the virtual source O_1 coincides with the radius of the circular arc; the same holds true for a_2. When computing a, according to the standard interpolation of the nodal values a_i and a_2, using formula (13), we obtain $a = a_1 = a_2$. However, for points inside the infinite element, along the discrete approximation Γ^h of the envelope Γ, the distance from the center of the circular arc is not a. This situation is equivalent to defining an interpolated virtual source location for points on Γ^h at distance a from Γ^h along the radial direction (see Figure B.15). In other words, when using formulas (12) and (13) to compute ξ and a the interpolated locations of the virtual sources do not coincide with the center of the arc O. This means that relationship (21) is valid, in general, only along the infinite edges, even when the virtual sources relative to all the infinite edges coincide with the center of radiation. The effects of this fact on the quality of the approximation are analyzed in Section 5.1.1.

Appendix C. Time stability conditions for the Astley-Leis formulation

Appendix C.1. Conditions for positive semi-definiteness of $\mathbf{M}$

First of all, we show that, if the mass matrix relative to the infinite domain, $\mathbf{M_{IE}} \in \mathbb{R}^{n_{\mathrm{IE}} \times n_{\mathrm{IE}}}$ (where n_{IE} is the number of DOFs associated with the infinite elements) is positive semi-definite, then the global mass matrix $\mathbf{M}$ is also positive semi-definite. Let's consider a generic vector $\mathbf{y} \in \mathbb{R}^{n_{\mathrm{DOF}}}$:

$$\mathbf{y}^\top \mathbf{M} \mathbf{y} = \mathbf{y_{FE}}^\top \mathbf{M_{FE}}\, \mathbf{y_{FE}} + \mathbf{y_{IE}}^\top \mathbf{M_{IE}}\, \mathbf{y_{IE}} \geq 0, \tag{C.1}$$

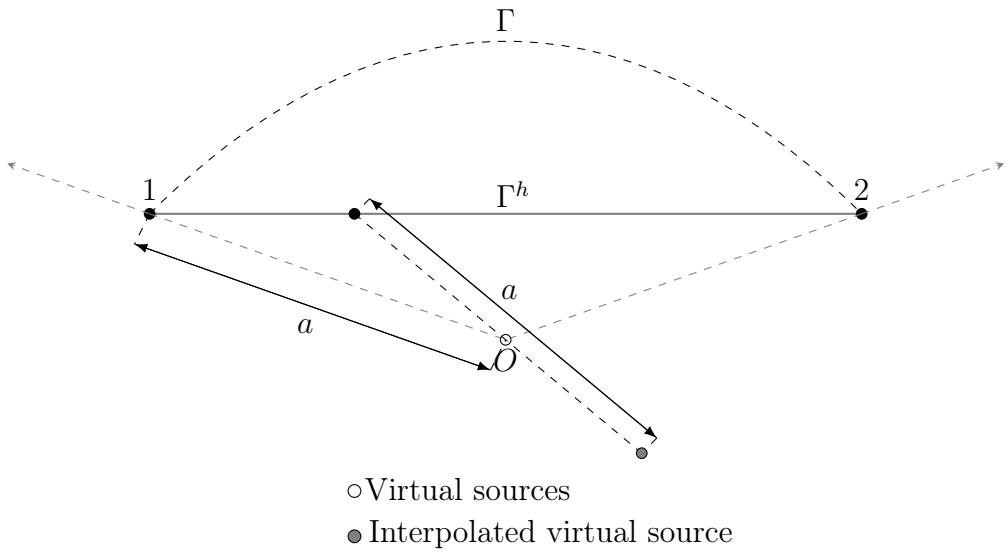

Figure B.15: Schematic representation of an infinite element. The envelope Γ is a circle, and it is discretized with a piecewise linear envelope Γ^h. The virtual sources relative to the nodes 1 and 2 coincide with the center of the arc O. The interpolated virtual sources relative to the other points on Γ^h do not coincide with the center of the arc O.

where the subscripts $_{\mathrm{FE}}$ and $_{\mathrm{IE}}$ denote the DOFs associated with the finite and the infinite elements, respectively; the last inequality in (C.1) comes from the fact that $\mathbf{M_{IE}} \geq 0$ by hypothesis and $\mathbf{M_{FE}} \geq 0$ when standard polynomial shape functions are used and the material properties of the medium in which sound propagates are physically realizable. The inequality in (C.1) is valid for any vector $\mathbf{y} \in \mathbb{R}^{n_{\mathrm{DOF}}}$, which means, by definition of positive semi-definite matrix, that $\mathbf{M} \geq 0$.

Appendix C.2. Conditions for positive semi-definiteness of $\mathbf{M_{IE}}$

Next, we show that $\mathbf{M_{IE}} \geq 0$, provided that the element mass matrix $\mathbf{M^e_{IE}} \in \mathbb{R}^{n_{\mathrm{IE}} \times n_{\mathrm{IE}}}$ is positive semi-definite for all the infinite elements. Let's consider a generic vector $\mathbf{y_{IE}} \in \mathbb{R}^{n_{\mathrm{IE}}}$:

$$\mathbf{y_{IE}}^\top \mathbf{M_{IE}} \mathbf{y_{IE}} = \mathbf{y^1_{IE}}^\top \mathbf{M^1_{IE}}\, \mathbf{y^1_{IE}} + ... + \mathbf{y^{n_E}_{IE}}^\top \mathbf{M^{n_E}_{IE}}\, \mathbf{y^{n_E}_{IE}} \geq 0, \tag{C.2}$$

where n_{E} is the number of infinite elements, and the inequality comes from the fact that $\mathbf{M^e_{IE}} \geq 0$ by hypothesis, with $e = 1, ..., n_{\mathrm{E}}$. By definition of positive semi-definite matrix, inequality (C.2) implies $\mathbf{M_{IE}} \geq 0$.

Appendix C.3. Condition for positive semi-definiteness of $\mathbf{M}^e_{\mathbf{IE}}$

We now analyze under which conditions $\mathbf{M}^e_{\mathbf{IE}} \geq 0$. In the Astley-Leis formulation, when the test basis functions are taken as the weighted complex conjugate of the shape functions, $\mathbf{M}^e_{\mathbf{IE}}$ takes the form (see [13]):

$$\mathbf{M}^e_{\mathbf{IE}} = \int_\Omega \left\{ \frac{1}{c^2} w \boldsymbol{\psi}^\top \boldsymbol{\psi} \left[1 - \|\nabla_x \mu\|^2 \right] \right\} \mathrm{d}\Omega, \tag{C.3}$$

where c is the speed of sound. To make it easier to analyze its definiteness, we rewrite it in a much simpler form. In particular, when using Gauss quadrature formulas to perform the integration, expression (C.3) can be rewritten as

$$\mathbf{M}^e_{\mathbf{IE}} = \boldsymbol{\psi}^\top \mathbf{D}^e \boldsymbol{\psi}, \tag{C.4}$$

where $\boldsymbol{\psi} \in \mathbb{R}^{n_{\mathrm{IE}} \times n_g}$ is the matrix of polynomial functions, evaluated at the Gauss points:

$$\boldsymbol{\psi} = \begin{pmatrix} \boldsymbol{\psi}(\mathbf{g}_1) \\ \vdots \\ \boldsymbol{\psi}(\mathbf{g}_{ng}) \end{pmatrix}, \tag{C.5}$$

n_g is the number of Gauss points, $\mathbf{g}_j = (s^g_j, t^g_j, v^g_j)$, is the vector of parent element coordinates of the j-th Gauss point and $\mathbf{D}^e$ is a diagonal matrix, whose j-th component along the diagonal is

$$\mathbf{D}^e_{jj} = \frac{1}{c^2} g^w_j \cdot \det \mathbf{J}_j \left[1 - \|\nabla_x \mu(\mathbf{g}_j)\| \right] w(\mathbf{g}_j), \tag{C.6}$$

where g^w_j is the j-th Gauss weight and $\det \mathbf{J}_j$ is the determinant of the Jacobian of the transformation between physical and parent element coordinates, evaluated at the j-th Gauss point.

Since $\mathbf{D}^e$ is a diagonal matrix, it is positive semi-definite if and only if all its components are not smaller than zero. This happens if and only if

$$\|\nabla_x \mu(\mathbf{g}_j)\| \leq 1 \; \forall i, i = 1, ..., n_g. \tag{C.7}$$

We show that if $\mathbf{D}^e \geq 0$ then $\mathbf{M}^e_{\mathbf{IE}} \geq 0$. Let's choose a generic vector $\mathbf{y} \in \mathbb{R}^n$:

$$\mathbf{y}^\top \mathbf{M}^e_{\mathbf{IE}} \mathbf{y} = \mathbf{y}^\top \left(\boldsymbol{\psi}^\top \mathbf{D}^e \boldsymbol{\psi} \right) \mathbf{y} = (\boldsymbol{\psi}\mathbf{y})^\top \mathbf{D}^e (\boldsymbol{\psi}\mathbf{y}) = \mathbf{z}^\top \mathbf{D}^e \mathbf{z} \geq 0, \tag{C.8}$$

where the last inequality in (C.8) comes from the fact that $\mathbf{D}^e \geq 0$ by hypothesis, with $\mathbf{z} = \boldsymbol{\psi}\mathbf{y} \in \mathbb{R}^{n_g}$. This proves that $\mathbf{D}^e \geq 0$ implies $\mathbf{M}^e_{\mathbf{IE}} \geq 0$.

Appendix C.4. Behavior of $\|\nabla_x \mu\|$

Let's define $\boldsymbol{\xi}(s,t,v)$ as the vector pointing in the direction orthogonal to the envelope Γ, with magnitude $\xi(s,t,v)$:

$$\boldsymbol{\xi}(s,t,v) = \mathbf{n}(s,t)\xi(s,t,v), \tag{C.9}$$

where $\mathbf{n}(s,t)$ is the unit vector normal to the envelope Γ at the point identified by the parent element coordinates $(s,t,v=-1)$. For the classical Astley-Leis formulation, the phase distance μ is defined in (16); after differentiating with respect to ξ, we obtain

$$\frac{\partial \mu}{\partial \xi} = 1. \tag{C.10}$$

Additionally, for the properties of the gradient operator, thanks to the relationship between the gradient of a function and its directional derivatives, we have:

$$\nabla_x \mu \cdot \boldsymbol{\xi} = \frac{\partial \mu}{\partial \xi}\xi. \tag{C.11}$$

Let's consider the ideal scenario where the envelope Γ is represented exactly and no error arises from the geometrical discretization, and let's choose the infinite edges in the e-th element to be extruded orthogonally to the envelope Γ. In this case, $\mu(s,t,v)$ represents the distance between the point with physical coordinates $\mathbf{x}(s,t,v)$ and Γ. As such, the lines with constant μ are perpendicular to $\mathbf{n}(s,t)$. This means that $\nabla_x \mu(s,t,v)$, which, for the properties of the gradient operator, is perpendicular to the μ iso-lines, is parallel to $\mathbf{n}(s,t)$ and, as a consequence, aligned with $\boldsymbol{\xi}$. Thus, we can write

$$\nabla_x \mu(s,t,v) \cdot \boldsymbol{\xi}(s,t,v) = \|\nabla_x \mu(s,t,v)\| \xi(s,t,v). \tag{C.12}$$

Finally, inserting (C.11) and (C.10) in (C.12) and simplifying the resulting equation, we obtain

$$\|\nabla_x \mu(s,t,v)\| = \frac{\partial \mu}{\partial \xi}(s,t,v) = 1. \tag{C.13}$$

This means that, if the extrusion direction is orthogonal to the envelope Γ for all the infinite edges, we obtain $\|\nabla_x \mu\| = 1$ everywhere in the exterior domain, provided that no approximation errors arise from the discretization of Γ.

Appendix D. Behavior of $\|\nabla_{\boldsymbol{x}}\overline{\boldsymbol{\mu}}\|$ for flexible infinite elements

In this appendix, we study the behavior of $\|\nabla_x\overline{\mu}\|$ when the infinite edges in the e-th element are extruded in the direction orthogonal to the envelope Γ, as in the time-stable infinite elements proposed in [21]. For simplicity, we consider the two-dimensional case, but all the considerations made in this appendix hold in three dimensions. Let's consider a point on the envelope Γ,

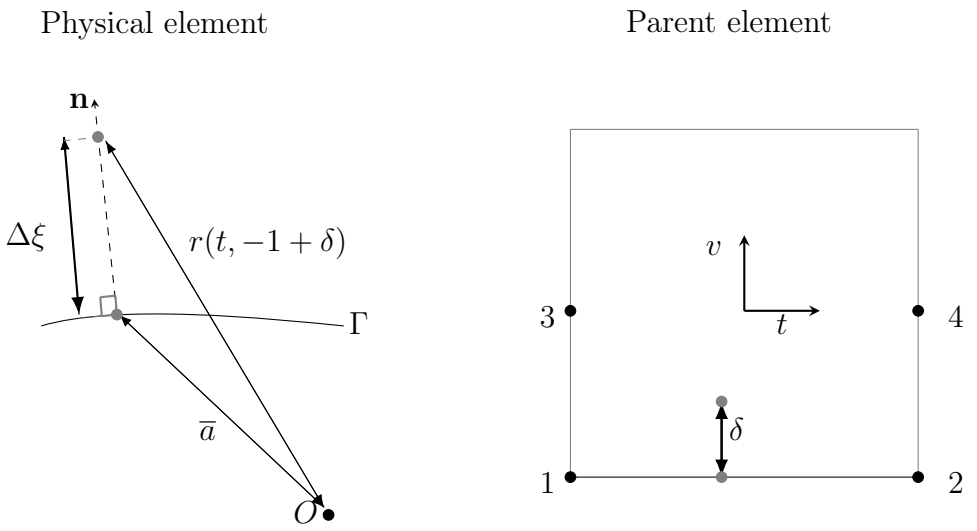

Figure D.16: Schematic representation of a region inside a flexible infinite element. The infinite edges are extruded orthogonally to the envelope Γ.

with parent element coordinates $(t, v = -1)$. First, we show that

$$\|\nabla_x\overline{\mu}(t, v = -1)\| \leq 1, \tag{D.1}$$

provided that the infinite edges in the element are aligned with the normal vector of the envelope Γ at the mapping nodes on Γ. For the properties of the gradient operator, thanks to the relationship between the gradient of a function and its directional derivatives, we have:

$$\nabla_x\overline{\mu}(t, -1) \cdot \boldsymbol{\xi}(t, -1) = \frac{\partial\overline{\mu}}{\partial\xi}(t, -1)a \tag{D.2}$$

The envelope Γ is an iso-line of $\overline{\mu}$, with $\overline{\mu} = 0$ by definition. It follows

$$\|\nabla_x\overline{\mu}(t, -1)\| = \frac{\partial\overline{\mu}}{\partial\xi}(t, -1), \tag{D.3}$$

since the gradient of $\overline{\mu}$ is perpendicular to the iso-lines of $\overline{\mu}$. Let's define

$$\Delta\xi(\delta) = \xi(v = -1 + \delta) - a, \tag{D.4}$$

and

$$\Delta r(\delta) = r(v = -1 + \delta) - \overline{a}. \tag{D.5}$$

The partial derivative of $\overline{\mu}$ with respect to ξ can be written as

$$\frac{\partial \overline{\mu}}{\partial \xi}(t, -1) = \lim_{\delta \to 0} \frac{\Delta r(\delta)}{\Delta \xi(\delta)}. \tag{D.6}$$

By triangle inequality (see Figure D.16), we have

$$r(v = -1 + \delta) \leq \Delta\xi + \overline{a}, \tag{D.7}$$

from which follows

$$\Delta r \leq \Delta\xi. \tag{D.8}$$

As a consequence, we obtain

$$\frac{\partial \overline{\mu}}{\partial \xi}(t, -1) \leq 1. \tag{D.9}$$

Therefore, by plugging (D.9) into (D.3), we obtain

$$\|\nabla_x \overline{\mu}(t, -1)\| \leq 1. \tag{D.10}$$

Once again, as in the classical Astley-Leis formulation, small errors may arise because of the geometrical approximation. In this case, as in [21], we propose to neglect these small discrepancies to ensure the stability of the method.

For $v \to 1$, it is easy to show that $\Delta r \to \Delta\xi$ which implies

$$\lim_{v \to 1} \|\nabla_x \overline{\mu}\| \to 1. \tag{D.11}$$

In the region between $v = -1$ and $v \to 1$, we don't have any guarantee that $\|\nabla_x \overline{\mu}\| \leq 1$. The exact behavior of $\|\nabla_x \overline{\mu}\|$ depends on the geometry of the infinite element. Geometries for which $\|\nabla_x \overline{\mu}\| > 1$ for $v > 0$ are often encountered in practical applications.

References

[1] D. Givoli, Computational absorbing boundaries, in: Computational Acoustics of Noise Propagation in Fluids-Finite and boundary element methods, Springer, 2008, pp. 145–166.

[2] A. Bayliss, E. Turkel, Radiation boundary conditions for wave-like equations, Commun. Pure Appl. Math. 33 (1980) 707–725.

[3] J.-P. Berenger, A perfectly matched layer for the absorption of electromagnetic waves, J. Comput. Phys. 114 (1994) 185–200.

[4] U. Basu, A. K. Chopra, Perfectly matched layers for transient elastodynamics of unbounded domains, Int. J. Numer. Methods Eng. 59 (2004) 1039–1074.

[5] J. Diaz, P. Joly, A time domain analysis of pml models in acoustics, Comput. Methods Appl. Mech. Eng. 195 (2006) 3820–3853.

[6] Z. Chen, X. Wu, Long-time stability and convergence of the uniaxial perfectly matched layer method for time-domain acoustic scattering problems, SIAM J. Numer. Anal. 50 (2012) 2632–2655.

[7] A. Modave, A. Kameni, J. Lambrechts, E. Delhez, L. Pichon, C. Geuzaine, An optimum pml for scattering problems in the time domain, Eur. Phys. J.-Appl. Phys. 64 (2013) 24502.

[8] A. Modave, J. Lambrechts, C. Geuzaine, Perfectly matched layers for convex truncated domains with discontinuous galerkin time domain simulations, Comput. Math. Appl. 73 (2017) 684–700.

[9] S. Francois, H. Goh, L. F. Kallivokas, Non-convolutional second-order complex-frequency-shifted perfectly matched layers for transient elastic wave propagation, Comput. Methods Appl. Mech. Eng. 377 (2021) 113704.

[10] B. Kaltenbacher, M. Kaltenbacher, I. Sim, A modified and stable version of a perfectly matched layer technique for the 3-d second order wave equation in time domain with an application to aeroacoustics, J. Comput. Phys. 235 (2013) 407–422.

[11] P. Bettess, O. Zienkiewicz, Diffraction and refraction of surface waves using finite and infinite elements, Int. J. Numer. Methods Eng. 11 (1977) 1271–1290.

[12] K. Gerdes, The conjugated vs. the unconjugated infinite element method for the helmholtz equation in exterior domains, Comput. Methods Appl. Mech. Eng. 152 (1998) 125–145.

[13] R. Astley, G. Macaulay, J.-P. Coyette, L. Cremers, Three-dimensional wave-envelope elements of variable order for acoustic radiation and scattering. part i. formulation in the frequency domain, J. Acoust. Soc. Am. 103 (1998) 49–63.

[14] L. Cremers, K. Fyfe, J. Coyette, A variable order infinite acoustic wave envelope element, J. Sound Vib. 171 (1994) 483–508.

[15] O. Zienkiewicz, K. Bando, P. Bettess, C. Emson, T. Chiam, Mapped infinite elements for exterior wave problems, Int. J. Numer. Methods Eng. 21 (1985) 1229–1251.

[16] W. Eversman, Mapped infinite wave envelope elements for acoustic radiation in a uniformly moving medium, J. Sound Vib. 224 (1999) 665–687.

[17] D. S. Burnett, A three-dimensional acoustic infinite element based on a prolate spheroidal multipole expansion, J. Acoust. Soc. Am. 96 (1994) 2798–2816.

[18] D. S. Burnett, R. L. Holford, Prolate and oblate spheroidal acoustic infinite elements, Comput. Methods Appl. Mech. Eng. 158 (1998) 117–141.

[19] D. S. Burnett, R. L. Holford, An ellipsoidal acoustic infinite element, Comput. Methods Appl. Mech. Eng. 164 (1998) 49–76.

[20] R. Astley, G. Macaulay, J. Coyette, Mapped wave envelope elements for acoustical radiation and scattering, J. Sound Vib. 170 (1994) 97–118.

[21] R. Astley, J. Hamilton, The stability of infinite element schemes for transient wave problems, Comput. Methods Appl. Mech. Eng. 195 (2006) 3553–3571.

[22] C. H. Wilcox, A generalization of theorems of rellich and atkinson, Proc. Am. Math. Soc. 7 (1956) 271–276.

[23] R. Astley, Mapped spheroidal wave-envelope elements for unbounded wave problems, Int. J. Numer. Methods Eng. 41 (1998) 1235–1254.

[24] R. Astley, Transient spheroidal elements for unbounded wave problems, Comput. Methods Appl. Mech. Eng. 164 (1998) 3–15.

[25] R. Astley, Infinite elements for wave problems: a review of current formulations and an assessment of accuracy, Int. J. Numer. Methods Eng. 49 (2000) 951–976.

[26] R. Astley, J.-P. Coyette, The performance of spheroidal infinite elements, Int. J. Numer. Methods Eng. 52 (2001) 1379–1396.

[27] L. Li, J.-S. Sun, H. Sakamoto, A modified infinite element method for acoustic radiation, J. Comput. Acoust. 10 (2002) 113–121.

[28] L. Li, J. Sun, H. Sakamoto, On the virtual acoustical source in mapped infinite element, J. Sound Vib. 261 (2003) 945–951.

[29] L. Li, S. Kunimatsu, J.-S. Sun, H. Sakamoto, A new conjugated mapped infinite element, J. Comput. Acoust. 12 (2004) 543–570.

[30] L. Li, J.-S. Sun, H. Sakamoto, A generalized infinite element for acoustic radiation, J. Vib. Acoust. 127 (2005) 2–11.

[31] D. Dreyer, O. von Estorff, Improved conditioning of infinite elements for exterior acoustics, Int. J. Numer. Methods Eng. 58 (2003) 933–953.

[32] R. Astley, Transient wave envelope elements for wave problems, J. Sound Vib. 192 (1996) 245–261.

[33] R. Astley, J. Hamilton, Infinite elements for transient flow acoustics, in: 7th AIAA/CEAS Aeroacoustics Conference and Exhibit, 2001, p. 2273.

[34] R. Astley, J.-P. Coyette, L. Cremers, Three-dimensional wave-envelope elements of variable order for acoustic radiation and scattering. part ii. formulation in the time domain, J. Acoust. Soc. Am. 103 (1998) 64–72.

[35] S. van Ophem, O. Atak, E. Deckers, W. Desmet, Stable model order reduction for time-domain exterior vibro-acoustic finite element simulations, Comput. Methods Appl. Mech. Eng. 325 (2017) 240–264.

[36] D. Bizzarri, O. Atak, S. van Ophem, T. Tamarozzi, P. Jiranek, L. Scurria, A. Garcia de Miguel, M. Alvarez Blanco, K. Janssens, W. Desmet, Model order reduction and smart virtual sensing for unbounded vibro-acoustics using high order fem and infinite elements, in: Proceedings of the International Conference on Noise and Vibration Engineering (ISMA 2022), Leuven, Belgium, 2022.

[37] A. van de Walle, The power of model order reduction in vibroacoustics: And its applications in model-based sensing, Ph.D. thesis, KU Leuven, 2018.

[38] S. van Ophem, Novel reduction techniques for exterior vibro-acoustic models and their use in model-based sensing and identification, Ph.D. thesis, KU Leuven, 2019.

[39] S. van Ophem, B. Forrier, D. Bizzarri, O. Atak, A. de Miguel, M. Elkafafy, M. Dal Borgo, T. Tamarozzi, M. Alvarez Blanco, K. Janssens, et al., Physics-based virtual acoustic sensing for enhanced direct field acoustic excitation testing, in: Proceedings of the International Conference on Noise and Vibration Engineering (ISMA 2022), Leuven, Belgium, 2022.

[40] C. B. Barber, D. P. Dobkin, H. Huhdanpaa, The quickhull algorithm for convex hulls, ACM Trans. Math. Softw. (TOMS) 22 (1996) 469–483.

[41] R. J. Astley, Infinite elements, in: Computational Acoustics of Noise Propagation in Fluids-Finite and Boundary Element Methods, Springer, 2008, pp. 197–230.

[42] O. Zaleski, W.-C. von Karstedt, O. von Estorff, Zur modellierung mit boundary elementen und finiten elementen bei schallabstrahlungsberechnungen. 1. (on modeling with boundary elements and finite elements in sound radiation calculations. 1.), in: Deutschsprachige Anwender-Konferenz SYSNOISE, Bühlerhöhe, 1999.

[43] D. Dreyer, S. Petersen, O. von Estorff, Effectiveness and robustness of improved infinite elements for exterior acoustics, Comput. Methods Appl. Mech. Eng. 195 (2006) 3591–3607.

[44] R. Astley, J. Hamilton, Numerical studies of conjugated infinite elements for acoustical radiation, J. Comput. Acoust. 8 (2000) 1–24.

[45] D. Dreyer, Efficient Infinite Elements for Exterior Acoustics, Berichte aus der Akustik, Shaker, 2004.

[46] K. Gerdes, A review of infinite element methods for exterior helmholtz problems, J. Comput. Acoust. 8 (2000) 43–62.

[47] J. Cipolla, Acoustic infinite elements with improved robustness, in: Proceedings of ISMA, 2002, pp. 2181–2187.

[48] D. Bizzarri, H. Beriot, O. Atak, S. van Ophem, Enhancing vibroacoustic reduced order models for digital twin development in industrial applications, in: INTER-NOISE and NOISE-CON Congress and Conference Proceedings, volume 270, Institute of Noise Control Engineering, 2024, pp. 1029–1038.

[49] H. Bériot, A. Modave, An automatic perfectly matched layer for acoustic finite element simulations in convex domains of general shape, Int. J. Numer. Methods Eng. 122 (2021) 1239–1261.

[50] H. Bériot, A. Prinn, G. Gabard, Efficient implementation of high-order finite elements for helmholtz problems, Int. J. Numer. Methods Eng. 106 (2016) 213–240.

[51] H. Bériot, G. Gabard, Anisotropic adaptivity of the p-fem for time-harmonic acoustic wave propagation, J. Comput. Phys. 378 (2019) 234–256.

[52] J. Biermann, O. von Estorff, S. Petersen, C. Wenterodt, Higher order finite and infinite elements for the solution of helmholtz problems, Comput. Methods Appl. Mech. Eng. 198 (2009) 1171–1188.

[53] C. Geuzaine, J.-F. Remacle, Gmsh: A 3-d finite element mesh generator with built-in pre-and post-processing facilities, Int. J. Numer. Methods Eng. 79 (2009) 1309–1331.

[54] Siemens industry software simcenter nastran user's guide (version 2022.1), `https://docs.sw.siemens.com/en-US/doc/289054037/PL20201105151514625.xid1853788/xid1853789`, 2022.